TÉCNICO LISBOA

Assessment of the Numerical Properties of ReFRESCO: a Pressure-Based Compressible Flow Solver

Cristiano Miguel Filipe Silva

Thesis to obtain the Master of Science Degree in

Mechanical Engineering

Supervisors: Prof. Luís Rego da Cunha de Eça
MSc João Maria de Afonseca Portela Roseira Muralha

Examination Committee

Chairperson: Prof. José Manuel da Silva Chaves Ribeiro Pereira
Supervisor: Prof. Luís Rego da Cunha de Eça
Members of the Committee: Prof. João Carlos de Campos Henriques
Dr. Christiaan Marijn Klaij

January 2021

Acknowledgments

I would like to take his opportunity to express my most sincere gratitude towards the following people, whom helped and supported me throughout the development of this work:

To my supervisors, Professor Luis Eça and MSc João Muralha, for they gave me the chance to develop this work with guidance and were always prone to clarify any doubts I had.

To Dr. Christiaan M. Klaij, for the great insights and perspectives on the results obtained.

To my parents, sister and grandparents, for all the support they have been giving me during my all life.

To my girlfriend, Cristina Santos, without whom my days would be less colourful.

To my long time friends, André Parreira, Dorismar Filho, Gabriel Moura, Manuel Sousa and Ricardo Santos, for always keeping in touch with me despite each one of us have been following different paths.

Resumo

Esta tese avalia a robustez numérica (erros iterativos) e a precisão (erros de discretização) do algoritmo baseado na pressão para escoamentos compressíveis monofásicos, incluído no código ReFRESCO.
Os objetivos principais são: verificar a capacidade de reduzir erros iterativos para valores desprezíveis (robustez); estimar a ordem de convergência com o refinamento da malha (precisão) para quantidades de interesse integrais e locais e comparar as soluções do ReFRESCO com resultados de referência presentes na literatura.
Selecionaram-se dois conjuntos de casos: três com um escoamento bi-dimensional, subsónico e turbulento (sobre uma placa plana em gradiente de pressão nulo, sobre uma lomba e em torno do perfil alar NACA0012), definidos em NASA Turbulence Modeling Resource; e outros três, comuns na literatura, simulando um escoamento invíscido sobre um arco circular em condições subsónicas, transónicas e supersónicas.
Realizaram-se estudos de refinamento da malha para todos os casos, em conjuntos de malhas geometricamente semelhantes, permitindo uma estimativa consistente da ordem de convergência da malha.
Verificou-se a robustez do algoritmo, pois a maioria dos erros iterativos baixaram para valores próximos da precisão da máquina.
A convergência iterativa é fortemente influenciada pelo grau de refinamento da malha e pela solução da equação que corrige a pressão.
As ordens de convergência com o refinamento da malha estimadas dependem do caso de estudo, das quantidades de interesse e do nível de refinamento das malhas.
Os resultados do ReFRESCO acompanham as soluções encontradas na literatura de referência, mas revelam oscilações numéricas perto de choques, descontinuidades geométricas ou em malhas com elevada excentricidade.

Palavras-chave: Verificação de Soluções, Algoritmos baseados na pressão, Mecânica de Fluidos Computacional

Abstract

This work assesses the numerical robustness (iterative errors) and accuracy (discretization errors) of the single-phase, pressure-based compressible flow solver developed within the ReFRESCO CFD package. The objectives of the work are threefold: check the ability to reduce iterative errors to negligible levels (robustness); estimate the order of grid convergence (accuracy) for integral and local quantities of interest and compare ReFRESCO solutions with reference data available in the open literature.

Two sets of test cases are selected: three two-dimensional, subsonic, turbulent flows (zero pressure gradient flat plate flow, bump-in-channel and NACA 0012 airfoil) available at the NASA Turbulence Modeling Resource; three two-dimensional inviscid flows over a circular-arc (bump) that correspond to subsonic, transonic and supersonic conditions that have been addressed in the open literature.

Grid refinement studies have been performed for all test cases using sets of geometrically similar grids that allow a reliable estimation of the observed order of grid convergence. The robustness of the code is demonstrated since iterative errors can be reduced to values close to machine accuracy for (almost) all test cases. Iterative convergence is strongly dependent on grid density and the solution of the pressure correction equation plays a crucial role in the robustness of the solution procedure.

Observed orders of grid convergence depends on the test case, selected quantity of interest and grid refinement level. ReFRESCO results are consistent with the reference data available in the open literature, but numerical oscillations can appear at shocks, geometric discontinuities or poor quality (large eccentricity) grids.

Keywords: Solution Verification, Pressure-based solvers, Computational Fluid Dynamics

Contents

List of Tables

List of Figures

Nomenclature

2D Two-dimensional

bJacobi Block Jacobi preconditioner

CDS Central-differences scheme

CFD Computational Fluid Dynamics

FANS Favre-Averaged Navier Stokes

FVM Finite Volume Method

GMRES Generalized Minimal Residual

HARM Fromm scheme with the harmonic limiter

MARIN Maritime Research Institute Netherlands

PDE Partial Differential Equations

QUICK Quadratic Upstream Interpolation for Convective Kinematics

RANS Reynolds-Averaged Navier Stokes

SuperLU Direct solver with complete LU factorization

TVD Total Variance Diminishing

UP First-order upwind scheme

Greek symbols

α Angle of attack

α_e Explicit under-relaxation factor

α_i Implicit under-relaxation factor

δ_{ij} Kronecker delta

ϵ Specific rate of dissipation of turbulence kinetic energy

ϵ_o Estimate of discretization error

γ Heat capacity ratio

$\hat{\nu_t}$ Undamped kinematic eddy viscosity

μ Molecular viscosity

μ_t Eddy viscosity

ω Rate of conversion of turbulence kinetic energy into thermal energy per volume and time unit

ϕ Undefined variable

ϕ_{exact} Exact solution

ϕ_o Estimate of exact solution

ρ Density

τ_{ij} Stress tensor

Roman symbols

A Matrix of coefficients

a, a_1, a_2 Error constants

a_P Coefficient of an arbitrary node P

a_{nb} Coefficient of neighbouring nodes nb

B Column vector of independent terms

b Independent term

c Chord

C_D Total drag coefficient

C_f Skin friction coefficient

C_L Lift coefficient

C_P Pressure coefficient

c_p Specific-heat coefficient at constant pressure

c_v Specific-heat coefficient at constant volume

C_X Horizontal force coefficient

C_{D_p} Pressure drag coefficient

C_{D_v} Viscous drag coefficient

E Total energy

e Specific internal energy

f_{v1} Empirical function

H Total enthalpy

h Specific enthalpy

h_i Cell size of grid i

k Turbulence kinetic energy

k_T Thermal conductivity

L Length

Ma Mach number

P Pressure

p Pressure relative to the hydrostatic pressure, observed order of grid convergence

P_o Stagnation pressure

Pr_t Turbulent Prandtl number

q_j Heat flux transfer

R Gas constant

r_i Grid refinement ratio

Re Reynolds number

T Temperature

t Time

T_o Stagnation temperature

U Velocity magnitude

u Velocity

U_ϕ Numerical uncertainty

Subscripts

i, j, k Computational indexes

x, y, z Cartesian coordinates

ref Reference condition

Superscripts

$\overline{\phi}$ Reynolds-average

ϕ' Fluctuation around the Favre-average

ϕ" Fluctuation around the Reynolds-average

$\tilde{\phi}$ Favre-average

Chapter 1

Introduction

Nowadays, Computational Fluid Dynamics (CFD) is far from a numerical tool exclusive for the aeronautics and aerospace industries [1], as it can be found scattered across other engineering fields, from marine and automotive to building and power generation, to mention a few [2]. In CFD, a numerical method is developed to simulate a fluid flow behaviour in a desired application, whether it is on a combustion chamber, over a wing, and so on. The governing equations of fluid motion are a system of partial differential equations (PDE) composed by the Navier-Stokes equations, which represent the conservation laws of mass and momentum. However, due to their complexity they are only analytically solved for simple cases [3].

One discretization technique typically employed is the Finite Volume Method (FVM), which transforms the governing flow PDE into algebraic equations by dividing the domain of interest in finite volumes [2]. The choice of primary flow variables, i.e., variables that are directly computed from the PDE, further categorizes these numerical algorithms. Two possible alternatives are: density-based and pressure-based solvers [4].

Density-based solvers were originally developed for high-speed compressible flows [5]. The continuity equation is a direct equation for density, and pressure is obtained from an equation of state, typically the perfect gas law. In contrast with pressure-based solution techniques, which were first employed in incompressible flows [6, 7], the mass conservation equation is modified and combined with with momentum to yield an equation for pressure [2].

Computing pressure from the continuity equation over density has attracted many research efforts, like [4, 8, 9] to mention a few. The reason for that is related with physical aspects that are commonly referred to in the literature by the dual role of pressure. As explained in [4], in low-speed flows, pressure acts exclusively on the velocity field to enforce mass conservation since density is constant. On the other hand, in high-Mach number flows, velocity variations are small compared to the flow's velocity magnitude, which means that pressure mainly acts on density to satisfy mass conservation. At intermediate-speed flows, pressure acts on velocity and density alike. Thus, changes in pressure are finite and relevant throughout all speeds, making this flow quantity very interesting to consider as the main variable in all-speed flow algorithms [10].

The recoding necessary for pressure-based incompressible solvers to handle compressible flows is well documented in key literature of the field, like in [2, 11]. Meanwhile, pseudo compressibility techniques and preconditioning methods had to be developed for density-based solvers to achieve same levels of versatility [12, 13].

Recently, a compressible version of ReFRESCO was presented [14, 15]. ReFRESCO is a CFD code designed for naval and offshore applications developed by MARIN (Maritime Research Institute Netherlands), in collaboration with other organizations around the world [16]. Most common practical problems in the Naval engineering field consider fluid incompressibility since the working fluid is water. However, certain applications like slamming or sloshing may involve multi-phase flows, where compressibility effects of the gaseous phase might be relevant. Accurate capturing of such physical phenomenon is the end-goal of ReFRESCO update, which is comprised of various steps.

Firstly, in [14], the solver was updated to handle laminar subsonic flows of perfect gases. Recoding of the original code was essential, namely the pressure-correction equation, as well as the momentum and energy equation had to be updated to account for fluid compressibility. A Code Verification [17] exercise was performed, using the Method of the Manufactured Solutions, to guarantee that coding errors were non-existent. Moreover, second order of grid convergence was reported, which matched with the theoretical one for all flow variables.

Afterwards, a brief assessment of the numerical properties of compressible ReFRESCO was performed in [15]. In that study, two benchmark test cases were used: turbulent flow over a flat plate and over a bump. Both test cases were selected from NASA Langley Research Center Turbulence Modeling Resource webpage [18], which centralizes results from RANS-based solvers where CFD developers can compare and verify their algorithms. The authors reported the iterative convergence rate to increase when velocity, temperature, and density, were imposed at the inlet of the domain over total pressure and total temperature. However, the first boundary conditions imply undisturbed flow properties at the inlet of the domain which often results in larger domain sizes. Additionally, a Solution Verification [19] exercise to quantities of interest like the skin friction coefficient and the drag coefficient was performed through order of grid convergence properties. Despite the observed order of grid convergence being lower with ReFRESCO, its solutions were less sensitive to grid coarsening, when comparing with two other solvers, CFL3D and FUN3D.

This thesis follows up on the assessment of the numerical properties of ReFRESCO for compressible flows aiming at expanding their evaluation in more test cases than what has been done so far. More precisely, this work will focus on the following properties:

1. Robustness - by analysing the iterative convergence;
2. Accuracy – through order of grid convergence studies in Solution Verification exercises, according with [20], to local, integral, and surface flow quantities.

In total, simulations will be carried out on two sets of benchmark test cases: three two-dimensional (2D), subsonic, turbulent flows (flow over a flat plate with zero pressure gradient, over a bump-in-channel and over the NACA0012 airfoil); three 2D inviscid flows over a circular arc (bump) in subsonic, transonic

and supersonic conditions. The viscous test cases are taken from [18], while the other is commonly addressed in the literature [4, 9]. Since reference data is available in the literature for the selected cases, this thesis also features a code-to-code comparison with the solutions from ReFRESCO and those of other codes.

This thesis is structured as followed: Chapter 2 presents the mathematical and numerical formulations. Chapter 3 describes the selected test cases, while the results for the iterative convergence, order of grid convergence studies and code to code solution comparison are presented and discussed in Chapter 4. Finally, this thesis ends in Chapter 5 with the main conclusions.

Chapter 2

Mathematical and Numerical Model

2.1 Mathematical model

2.1.1 Governing equations

The system of equations (eqs. 2.1) describes a general fluid dynamics problem. It is composed by the Navier-Stokes equations (eq. 2.1b), as well as the mass (eq. 2.1a) and total energy (eq. 2.1c) conservation principle, hereby written for a single-phase, unsteady flow of a compressible fluid in their conservative form, and index notation as:

$$\frac{\partial \rho}{\partial t} + \frac{\partial}{\partial x_i}\left(\rho u_i\right) = 0 \ , \tag{2.1a}$$

$$\frac{\partial}{\partial t}\left(\rho u_i\right) + \frac{\partial}{\partial x_j}\left(\rho u_j u_i\right) = -\frac{\partial p}{\partial x_i} + \frac{\partial \tau_{ij}}{\partial x_j} \ , \tag{2.1b}$$

and

$$\frac{\partial \rho E}{\partial t} + \frac{\partial}{\partial x_j}\left[\rho u_j H\right] = -\frac{\partial q_j}{\partial x_j} + \frac{\partial}{\partial x_j}\left(u_i \tau_{ij}\right) \ . \tag{2.1c}$$

The different variables stand for the following: ρ is the density, u_i is the velocity along the i^{th} direction x_i, p is the pressure relative to hydrostatics, E is the total energy, and H the total enthalpy. The stress tensor, τ_{ij}, and heat flux transfer, q_j, are given by the Newtonian fluid hypothesis and the Fourier's Law, respectively, i.e.:

$$\tau_{ij} = \mu\left(\frac{\partial u_i}{\partial x_j} + \frac{\partial u_j}{\partial x_i}\right) - \frac{2}{3}\mu\left(\frac{\partial u_k}{\partial x_k}\right)\delta_{ij} \tag{2.2a}$$

and

$$q_j = -k_T \frac{\partial T}{\partial x_j} \ , \tag{2.2b}$$

where μ, k_T, and T, are the molecular viscosity, the thermal conductivity coefficient, and the fluid's temperature, respectively; δ_{ij} is the Kronecker delta.

Closure of the before-mentioned system is achieved with an equation of state. The ideal gas approx-

imation can be used for that purpose, which states that:

$$P = \rho R T \ , \tag{2.3}$$

being P the pressure (relative pressure + hydrostatic pressure) and R the gas constant. Additionally, considering a calorific perfect gas, the energy equation can be modified to be written only in terms of primitive flow variables ρ, u_i, T and p, as:

$$e = c_v T \tag{2.4a}$$

and

$$h = c_p T \ , \tag{2.4b}$$

with c_v and c_p being the specific-heat coefficients at constant volume and pressure, respectively, e the specific internal energy and h the specific enthalpy.

2.1.2 Governing equations in turbulent flows

Time-averaging procedures, like Reynolds-average and Favre-average, can be employed to statistically steady flows. However, for compressible flows, the Reynolds-Averaged Navier Stokes (RANS) equations yield higher complexity than the Favre-Averaged Navier Stokes (FANS) equations. As in the former, double and triple products of fluctuations of flow quantities arise. Before averaging, all flow quantities are split in a time average quantity, and a fluctuation around the mean value, according to Reynolds decomposition. Following [21], the tilde denotes mass-averaged (or Favre-averaged) flow quantities, and the overbar indicates conventional Reynolds-average variables:

$$u_i = \tilde{u}_i + u_i'' \ , \tag{2.5a}$$

$$\rho = \overline{\rho}_i + \rho_i' \ , \tag{2.5b}$$

$$p = \overline{p}_i + p_i' \tag{2.5c}$$

and

$$T = \overline{T}_i + T_i'' \ . \tag{2.5d}$$

In this thesis, the Favre-Averaged Navier-Stokes will be employed on all viscous flows test cases, which are written below for a statistically steady flow (eqs. 2.6), as well as the average form of stress tensor (2.7a) and heat flux vector (eq.2.6a):

$$\frac{\partial}{\partial x_i}\left(\overline{\rho}\tilde{u}_i\right) = 0 \ , \tag{2.6a}$$

$$\frac{\partial}{\partial x_j}\left(\overline{\rho}\tilde{u}_j\tilde{u}_i\right) = -\frac{\partial \overline{p}}{\partial x_i} + \frac{\partial}{\partial x_j}\left[\overline{\tau}_{ij} - \overline{\rho u_j'' u_i''}\right] \ , \tag{2.6b}$$

$$\frac{\partial}{\partial x_j}\left[\overline{\rho}\tilde{u}_j\left(c_p\tilde{T}+\frac{1}{2}\tilde{u}_i\tilde{u}_i\right)+\tilde{u}_j\frac{1}{2}\overline{\rho u_i'' u_i''}\right]= \\ \frac{\partial}{\partial x_j}\left[-\overline{q_j}-c_p\overline{\rho u_j'' T''}+\overline{\tau_{ij}u_i''}-\frac{1}{2}\overline{\rho u_j'' u_i'' u_i''}\right]+\frac{\partial}{\partial x_j}\left[\tilde{u}_i\left(\overline{\tau}_{ij}-\overline{\rho u_i'' u_j''}\right)\right] \ , \quad \text{(2.6c)}$$

$$\overline{\tau}_{ij}=\mu\left(\frac{\partial\tilde{u}_i}{\partial x_j}+\frac{\partial\tilde{u}_j}{\partial x_i}\right)-\frac{2}{3}\mu\frac{\partial\tilde{u}_k}{\partial x_k}\delta_{ij} \ , \quad \text{(2.7a)}$$

and

$$\overline{q}_j=-k_T\frac{\partial\tilde{T}}{\partial x_j}. \quad \text{(2.7b)}$$

Independently of the averaging technique, extra terms will always arise that showcase the inherent difficulty when handling turbulence. Similar to the original system of governing flow equations, extra equations/correlations are necessary to close this set of averaged-equations.

Firstly, in the momentum equations, an extra quantity appears due to the non-linear nature of the convection terms. Its physical interpretation is associated with the diffusion of linear momentum between the mean velocity field and the velocity fluctuations. This term is known as the Reynolds-stress tensor and its computation is referred to in the literature as turbulence modelling [22]. In this work, the Boussinesq approximation will be used to model the Reynolds-stress, which states:

$$-\overline{\rho u_j'' u_i''}=\mu_t\left(\frac{\partial\tilde{u}_i}{\partial x_j}+\frac{\partial\tilde{u}_j}{\partial x_i}\right)-\frac{2}{3}\mu_t\frac{\partial\tilde{u}_k}{\partial x_k}\delta_{ij}-\frac{2}{3}\overline{\rho}k\delta_{ij} \ , \quad \text{(2.8)}$$

where turbulence is characterized as an increase in diffusivity accounted for with the eddy viscosity parameter, μ_t, and $\overline{\rho}k$ is the turbulence kinetic energy ($\overline{\rho}k=(1/2)\,\overline{\rho u_i'' u_i''}$). For flows up to supersonic Mach numbers, $\overline{\rho}k$ is neglected as $\overline{p}\gg\overline{\rho}k$ [21].

Secondly, in the averaged-energy equation, three new terms appear. The turbulent heat flux vector will be modelled using Reynolds analogy (eq. 2.9), where Pr_t is the turbulent Prandtl number. The remaining two new terms, molecular diffusion ($\overline{\tau_{ij}u_i''}$) and turbulent transport ($\frac{1}{2}\overline{\rho u_j'' u_i'' u_i''}$), will be neglected, for they only become relevant at supersonic speeds or above [21].

$$c_p\overline{\rho u_j'' T''}=-\frac{\mu_t c_p}{Pr_t}\frac{\partial\tilde{T}}{\partial x_j} \quad \text{(2.9)}$$

Lastly, to completely close out the system, one unknown variable remains to be modelled, the eddy-viscosity introduced earlier. A variety of modelling procedures based on the Boussinesq hypothesis have been developed, and can be further categorized according to the number of differential equations by them required [2]:

- Zero equation models – No differential equations are applied, which means eddy viscosity is computed from an algebraic equation. For example, Prandlt's algebraic mixing length model [23];
- One equation models – Like the Spalart & Allmaras model [24] which solves one differential transport equation for the undamped kinematic eddy viscosity, $\hat{\nu}=\mu_t/(\rho f_{v1})$, where f_{v1} is an empirical function;

- Two equation models – that are more commonly used in CFD simulations for industrial applications [25]. Among others, the $k-\epsilon$ model, from Jones and Launder [26], and the $k-\omega$ model of Wilcox [27], solve two transport equations each. Adding to k, one solves a transport equation for ϵ, specific rate of dissipation of turbulence kinetic energy, while the other computes ω, which is the rate of conversion of turbulent kinetic energy into thermal energy per volume and time unit.

For all turbulent flow calculations in this work, the Spalart and Allmaras [24] model will be employed to close the system of equations. This one-equation turbulence model features a transport equation for undamped kinematic eddy viscosity, with no trip term for a statistically steady flow, defined as:

$$u_j \frac{\partial \hat{\nu}}{\partial x_j} = c_{b1}(1-f_{t2})\hat{S}\hat{\nu} - \left[c_{w1}f_w - \frac{c_{b1}}{\kappa^2}f_{t2}\right]\left(\frac{\hat{\nu}}{d}\right)^2 + \frac{1}{\sigma}\left[\frac{\partial}{\partial x_j}\left(\left(\frac{\mu}{\rho}+\hat{\nu}\right)\frac{\partial \hat{\nu}}{\partial x_j}\right) + c_{b2}\frac{\partial \hat{\nu}}{\partial x_i}\frac{\partial \hat{\nu}}{\partial x_j}\right] \quad (2.10)$$

The definitions of $\hat{S}$, f_{t2}, f_w, f_{t2} and d, as well as the values for the constants c_{b1}, c_{b2}, c_{w1}, κ and σ, are given in [28].

2.1.3 Boundary conditions

Integration of partial differential equations requires the use of boundary conditions in order to numerically define the finite domain's boundaries. Boundary conditions are equations that represent physical conditions or just simplify geometric constraints [29]. The boundary conditions employed on this thesis are addressed bellow.

Wall boundary conditions define the analysed object geometry, whether that may be a flat plate, a bump, or an airfoil profile. At the geometry's surface, either the no-slip or slip boundary were applied. The former implies the tangential velocity component to be equal to the wall velocity (which is zero for all cases), while the latter imposes zero shear stress on the wall. However, both the impermeability condition, which impose zero normal velocity components, and the adiabatic condition i.e., null normal temperature derivative, were used in all simulations. When viscosity effects are considered, the undamped eddy viscosity is set equal to zero, according to [28]. Lastly, pressure is extrapolated from the interior cells and density is computed from the equation of state (eq. 2.3).

Symmetry boundaries are an example of geometric boundaries that shorten the numerical domain. They are used to mirror the domain interest in regions where the solution of all flow variables is symmetrical [29]. This is mathematically described by setting to zero the velocity component normal to that boundary, as well as the normal derivatives of all remaining variables.

Two types of inflow boundaries were used:

- Fixed density, velocity, and temperature at the boundary faces, according to undisturbed flow conditions, which equates to Dirichlet boundaries. In addition, for viscous flow simulations, the Dirichlet condition for the turbulence model transport equations sets a value for $\hat{\nu}$, $\hat{\nu} = 3(\mu/\rho)$.

- Alternatively, both stagnation temperature and stagnation pressure can be imposed. Linking between those quantities and the primitive flow variables are established through isentropic relations

of an ideal gas, like:

$$T_o = T\left(1 + \frac{\gamma - 1}{2} Ma^2\right) , \tag{2.11a}$$

and

$$P_o = P\left(1 + \frac{\gamma - 1}{2} Ma^2\right)^{\frac{\gamma}{\gamma - 1}} , \tag{2.11b}$$

where T_o and P_o are the stagnation temperature and stagnation pressure, respectively, γ is the heat capacity ratio and Ma is the Mach number, defined in equation 2.12. Density is calculated to comply with the equation of state and the boundary condition for the turbulence modelling equals that of the previous alternative.

$$Ma = \frac{U}{a} , \tag{2.12}$$

where U is the velocity magnitude $\left(U = \sqrt{u_i^2 + u_j^2 + u_k^2}\right)$ and a the speed of sound in the medium, which for a perfect gas is taken as $\sqrt{\gamma RT}$.

At the outflow, usually the static pressure level is imposed, and density is computed from the equation of state (eq. 2.3). Moreover, the remaining variables are extrapolated from the inside of the domain with zero streamwise derivatives.

Farfield Riemann boundary condition takes the Riemann invariants of the Euler-equations characteristic waves to calculate the flow properties at the boundary. However, it is only suitable where no flow perturbations are felt, as it assumes the gradients of all variables to be approximately zero. Because no local viscosity effects are considered in the vicinity of this boundary, naturally, $\partial\hat{\nu}/\partial x_i$ is set equal to zero. The implementation of this type of boundary condition for pressure-based solvers has been discussed recently in [30].

2.2 Numerical Model

2.2.1 Flow solver

The code used for all simulations was a compressible version of ReFRESCO. In this state, ReFRESCO is a viscous compressible solver that discretizes the mathematical model (Navier Stokes equations supplemented with turbulence models) using the FVM formulation, with cell-centred collocated variables and a face-based implementation. The continuity equation is modified to yield an equation for pressure, and density is computed from the equation of state. Thus, a pressure-correction equation is constructed based on a SIMPLE-like algorithm, where velocity-pressure-density coupling follows that proposed in literature [2, 11]. As a result, an extra term, a convection-like term, appears in the pressure correction equation, which transforms it from a Poisson equation, in incompressible regime, into a convection-diffusion equation. The diffusive terms are weighted by a factor proportional to $1/Ma^2$.

The convection terms of all transport equations were linearized with Picard's method. As a result, 5 linear systems of equations, plus an algebraic equation for density, are obtained and solved with a segregated approach. The linearization of the convective fluxes, plus the uncoupling of the equations

and the deferred corrections, build up a non-linear residual. The solver's development itself is outside the scope of this work and more detailed descriptions of the discretization process and the SIMPLE-like algorithm are available in [31, 32].

2.2.2 Solution procedure

Following the Finite Volume Method formulation, the differential transport equations are solved in control volumes, or cells, that divide the entire domain. On the volume integration of convective, diffusive, transient, and source terms, the Gauss' divergence theorem is applied. As a result, the fluxes of the transported quantities are approximated in one point for each unique face of the control volume through the mid-point rule.

Since, in a collocated variable framework, the values of the dependent quantities are stored in the centre of each control volume, numerical schemes are needed to write the face's fluxes only in terms of cell values. The choice of numerical schemes has many implications regarding very important properties of the discretized equations, like stability, accuracy, and boundeness. Those are addressed on introductory subjects about Computational Fluid Dynamics and in central references of the field, such as [2, 33]. However, their implications are outside the aim of this work and will not be explained in detail here. Nonetheless, after the application of a discretization scheme, for an arbitrary cell P in the interior of the domain, a general linear equation can be written as:

$$a_P \phi_P + \sum_{nb} a_{nb} \phi_{nb} = b \, , \tag{2.13}$$

where a_P and a_{nb}[1] are coefficients, which values depend on the discretization scheme used, whereas ϕ_P and ϕ_{nb} are the values of a flow variable, and b represents all terms that are independent of unknown variables.

Applying the same procedure to all cells of the domain, a linear system of equations is constructed and it can be written as:

$$A\phi = B \, , \tag{2.14}$$

with the capital letters being a matrix/vector form of the corresponding variables in eq. 2.13 and ϕ the solution vector for the desired flow variable.

2.2.3 Iterative convergence criteria

At maximum, five linear systems of equations, like eq. 2.14, are required to obtain the field solution. The x and y momentum balance, pressure correction, energy conservation, and $\tilde{\nu}$, transport equations were preferably solved using the Generalized Minimal Residual (GMRES) method with the block Jacobi (bJacobi) preconditioner [34]. However, some simulations required a more robust method to obtain a negligible influence of the iterative error and the direct LU factorization of the coefficient matrixes was used.

[1] nb subscript represents the neighbouring cells of an arbitrary cell P

Nonetheless, the stopping criteria for the iterative convergence were:

- For the linear problem, iterative convergence was achieved when the residual dropped two orders of magnitude. Adding to that, the maximum number of iterations for each linear system of equations was set equal to 200, except for the pressure correction equation (ΔP) where the limit was extended to 5000.
- For the non-linear problem, iterative convergence criteria were always based on the L_∞ norm of the normalized residuals of all transport equations. The normalization is done with the main diagonal values of the A matrixes (eq. 2.14) and the reference values in each test case: undisturbed flow conditions and reference length. A converged solution means that the value of the L_∞ is bellow 10^{-8}.

The majority of simulations were converged in a workstation with 16 processors. Occasionally a 56 processor computer was also used.

2.2.4 Relaxations

Under-relaxation parameters are commonly applied to improve convergence properties of CFD solvers as they enhance the robustness of the solution procedure. Both explicit and implicit relaxations were used in the present numerical simulations. The former improves the diagonal dominance characteristics of the linear system, while the latter influences the change in the linear system variables between consecutive iterations.

2.2.5 Discretization schemes

Throughout this thesis, different numerical schemes were used to approximate convective fluxes. Among the selected ones there are: second-order Total Variance Diminishing (TVD) Fromm scheme with the harmonic limiter (HARM) [35], second-order limited QUICK scheme [36] and a blending of the central-differences scheme (CDS) with 10% first-order upwind scheme (UP). The diffusive fluxes were always discretized with the central-differences scheme including non-orthogonality and eccentricity corrections. Lastly, the Gauss' theorem is used to determine the gradient of dependent variables at the cell centres. To avoid repetition, the convection schemes used in each test case were the following:

- In the flat plate and NACA0012 test cases, the Fromm scheme with the harmonic limiter was used;
- The limited QUICK scheme is present in all simulations of a viscous flow over a bump;
- Four convection schemes were used in the inviscid bump test cases: CDS blended with 10% UP, fully UP, HARM and QUICK schemes.

Chapter 3

Test cases

3.1 Test cases

As mentioned in Chapter 1, this thesis aims for an assessment of the numerical properties of ReFRESCO for compressible flows. For that purpose, two sets of test cases were chosen from the literature. The first one is composed of three viscous flow test cases and were selected from NASA Langley Research Center Turbulence Modeling Resource website [18]. The second set feature three inviscid flow test cases over a circular-arc (bump) in subsonic, transonic and supersonic conditions that were taken from the works of [4, 9]. Due to the number of test cases analysed, for language simplicity, common traits among them are hereby presented.

Grid presentation

Establishing a domain's dimensions and boundaries is not enough to solve a fluids dynamics problem numerically under the Finite Volume Method framework, for it requires converting the continuous PDE into a set of algebraic equations. These algebraic equations are obtained by decomposing the domain in a grid of elements, or cells, and relating the values of a flow quantity in a cell with its neighbouring ones.

The shape, orientation, dimensions, etc, of these elements distinguish one grid from another. Since grid's characteristics have a direct impact on the numerical properties of a solver [37], more than one type of grid was used throughout this work. Furthermore, as Solution Verification exercises, like observed order of grid convergence studies, require at least three geometrically similar grids with different refinement levels (see section 3.2), gathering these grids in sets was inevitable. Each grid is completely identified not only by its set, which will be set N for grids directly taken from [18], or set IM, for grids generated with in-house tools [38], but also by its grid refinement ratio, r_i, within their set that is defined by:

$$r_i = \frac{h_i}{h_1} = \left(\frac{N_{cells,1}}{N_{cells,i}}\right)^{\frac{1}{2}} = \frac{N_{wall,1}}{N_{wall,i}} \ , \tag{3.1}$$

where h_i is the typical cell size of grid i, N_{cells} the total number of grid cells, and N_{wall} the number of cells in the wall boundary. The subscript 1 refers to the finest grid of each set. Therefore, a grid with twice the refinement ratio has half the number of cells discretizing the tested object geometry.

Fluid properties

The working fluid for all simulations is assumed to be a perfect gas with gas constant of $R = 287.058 m^2/(s^2 K)$ and a heat capacity ratio of $\gamma = 1.4$. Furthermore, for viscous flows test cases, non-dimensional quantities like, Prandtl (eq. 3.2a) and turbulent Prandtl numbers, are taken as 0.72 and 0.9, respectively. Despite varying between each case both Reynolds (eq. 3.2b) are also presented below. Finally, the reference temperature is constantly considered equal to $T_{ref} = 300K$ and $c_p = 1004.703 J/(kgK)$.

$$Pr = \frac{c_p \mu}{k_T} \ , \tag{3.2a}$$

and

$$Re_x = \frac{\rho U x}{\mu} \ . \tag{3.2b}$$

3.1.1 Viscous flow

2D Zero Pressure Gradient Flat Plate

Figure 3.1 illustrates the domains dimensions and boundary conditions for the 2D turbulent flow over a flat plate with zero pressure gradient test case taken from [39].

For this test case, unitary density was assumed. Molecular viscosity is such that the Reynolds number, based on a reference length $L = 1m$, is $Re = 5 \times 10^6$, where the reference velocity magnitude was taken from the undisturbed Mach number of $Ma = 0.2$ using a reference temperature of $T_{ref} = 300K$.

The plate begins at the origin of the x-axis and extends to $x = 2L$, thus $Re_{2L} = 10^7$. Next, the inlet of the domain is located further upstream, at $x = -0.33m$, whereas its outlet coincides with the end of the plate. The total height was set one meter away from the plate, so no flow perturbations near the top boundary condition are expected [39].

Following figure 3.1, the case study boundary conditions are:

- Prescribed stagnation conditions (pressure and temperature) at the inlet;
- Pressure boundary condition at the outlet;
- Impermeable adiabatic surface with the no-slip condition on the entire plate;
- Symmetry boundary between the plate leading edge and the inlet;
- Farfield Riemann condition on the top boundary.

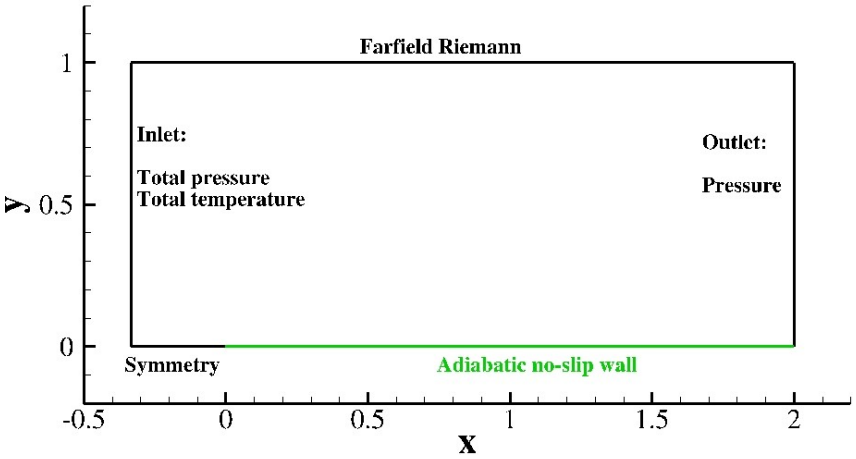

Figure 3.1: Domain and boundary conditions according to [18] for the calculation of the two-dimensional flow over a flat plate.

For this test case, two sets of geometrically similar grids were used. A set of five Cartesian grids, set N, and a set of five orthogonal multi-block grids, set IM. Moreover, both sets have a fixed refinement ratio of $r_i = 2$ between each consecutive grid. However, two extra grids, one between the two most refined grids and another twice as coarse, were added in both sets in order to improve the reliability of the grid convergence properties evaluation.

Figure 3.2 illustrates the coarsest grid of both set and table 3.1 summarizes information regarding N_{cells}, N_{wall}, y^+_{max}, and r_i, for the grids of this test case. The grids of set IM have slightly higher number of cells as their set N counterpart, but the y^+ was kept similar between each set and smaller or close to one, which is appropriate for the Spalart and Allmaras turbulence model [37]. Among the visual mismatches between the two grids is included the refinement at the leading edge of the plate, which is higher for the IM set and in a C shape. However, both sets have a grid orthogonal to the plate.

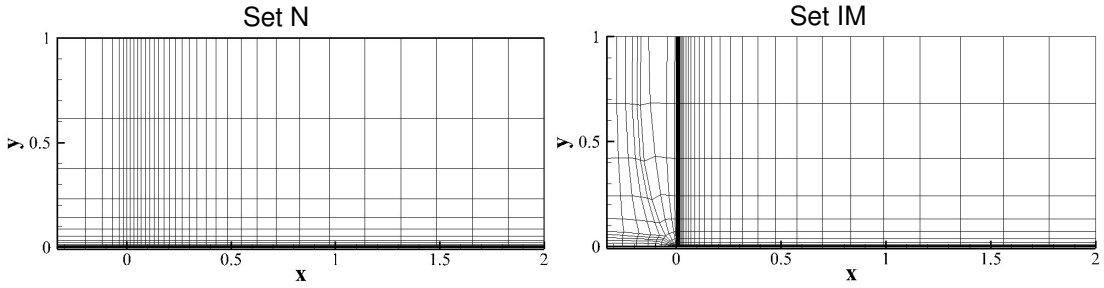

Figure 3.2: Illustration of the coarsest grids ($r_i = 16$) of grid sets N and IM. Two-dimensional flow over a flat plate.

2D Bump-in-channel

The viscous bump test case is another problem taken from [40].

The uniform flow's Mach number is equal to $Ma = 0.2$, based on the reference temperature $T_{ref} = 300K$, and the Reynolds number is $Re = 3 \times 10^6$, using both unitary length and density. The reference pressure is $P_{ref} = 86100Pa$.

Table 3.1: Total number of cells N_{cells}, number of boundary faces in the bump N_{wall} and grid refinement ratio r_i of the grids used. Two dimensional flow over a flat plate.

	Set N				Set IM			
Grid	r_i	N_{cells}	N_{wall}	y^+_{max}	r_i	N_{cells}	N_{wall}	y^+_{max}
1	1.00	208 896	448	0.127	1.00	256 000	640	0.125
1b	1.45	98 736	308	0.168	1.43	125 440	448	0.165
2	2.00	52 224	224	0.214	2.00	64 000	320	0.215
2b	2.90	24 684	154	0.285	2.86	31 360	224	0.286
3	4.00	13 056	112	0.365	4.00	16 000	160	0.377
4	8.00	3 264	56	0.632	8.00	4 000	80	0.686
5	16.0	816	28	1.16	16.0	1 000	40	1.35

Domain dimensions along with boundary conditions are presented in figure 3.3. The tested object geometry starts at the origin of the x-axis as a horizontal plate and its length defines the reference length of this case, i.e., $L_{ref} = 1.5m$. The actual bump is from $x = 0.3m$ to $x = 1.2m$ and is mathematically defined as:

$$y = 0.05 \left[\sin\left(\frac{10x}{9}\pi - \frac{\pi}{3} \right) \right]^4 \; for \; 0.3 \leq x \leq 1.2 \; . \tag{3.3}$$

Finally, the inlet and outlet are located 25 meters away from the beginning and ending of the object, respectively, and the top boundary is five meters high from the lower boundary.

The boundary conditions for this test follow the ones proposed at [40]. At the inlet, stagnation temperature and stagnation pressure is prescribed, while static pressure is imposed at the outflow. The no-slip adiabatic condition was considered on the plate+bump surface. Lastly, symmetry planes are used in the upper side of the domain and in the remaining lower boundary.

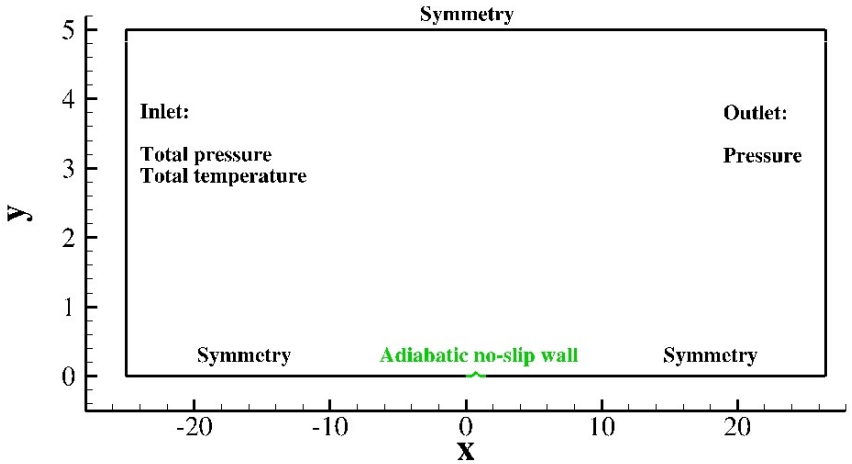

Figure 3.3: Domain and boundary conditions according to [18] for the calculation of the two-dimensional viscous flow over a bump.

The results for this test case were obtained in only one grid set, set N, from [41], which features 5 non-uniformly spaced grids. The vertical grid lines are clustered in the plate leading and trailing edges. On the other hand, the streamwise grid lines are parallel to the solid surface (plate+bump), stretched in

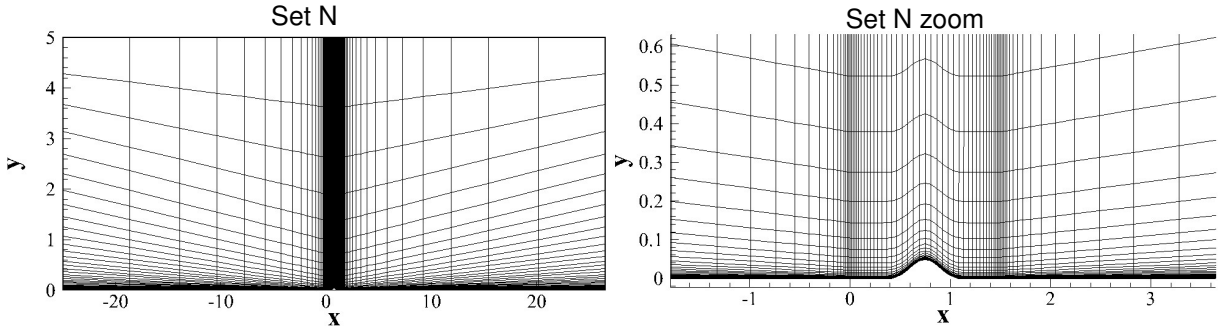

Figure 3.4: Illustration of the coarsest grids ($r_i = 16$) of set N. Two-dimensional viscous flow over a bump.

the vertical direction and clustered in the near-wall region, which extends to the wake, downstream of the bump. Table 3.2 and figure 3.4 present some information about each grid and an illustration of the coarsest grid, along with a zoom of solid surface, respectively.

A preliminary simulation was carried out using a grid locally orthogonal to the entire wall surface which resulted in spurious oscillations close to the bump's peak. These anomalies were attributed to the topology of the grid in that region and are presented in appendix A.

Table 3.2: Total number of cells N_{cells}, number of boundary faces in the solid surface N_{wall} and grid refinement ratio r_i of the grids used. Two dimensional viscous flow over a bump.

	Set N			
Grid	r_i	N_{cells}	N_{wall}	y^+_{max}
1	1.00	901 120	640	0.090
2	2.00	225 280	320	0.152
3	4.00	56 320	160	0.256
4	8.00	14 080	80	0.430
5	16.0	3 520	40	0.753

2D NACA0012 Airfoil

The final test case of the first set is the flow around a NACA0012 airfoil. The airfoil mathematical definition was slightly modified so that its chord, c, equals to $1m$ as explained in [42], and the no-slip adiabatic wall boundary condition was applied on the surface of the airfoil. The C-shaped domain illustrated in figure 3.5 has the farfield Riemann boundary condition applied $500m$ away from the airfoil surface. As far as incoming flow conditions are concerned, the chord-based Reynolds equates to six million, for $\rho_{ref} = 2.1264kg/m^3$, and the undisturbed Mach number is $Ma = 0.15$, so the flow is essentially incompressible. Simulations were performed for three incoming flow angle of attack, α, 0^o, 10^o and 15^o.

Only one grid set, set N, will be used and it was taken from at [43]. It is composed of 5 grids with a fixed grid refinement ratio of 2 between each one. Figure 3.6 depicts the coarsest grid and a zoom around the airfoil shape. All grids share a clustering of cells at the leading and trailing edges, which is

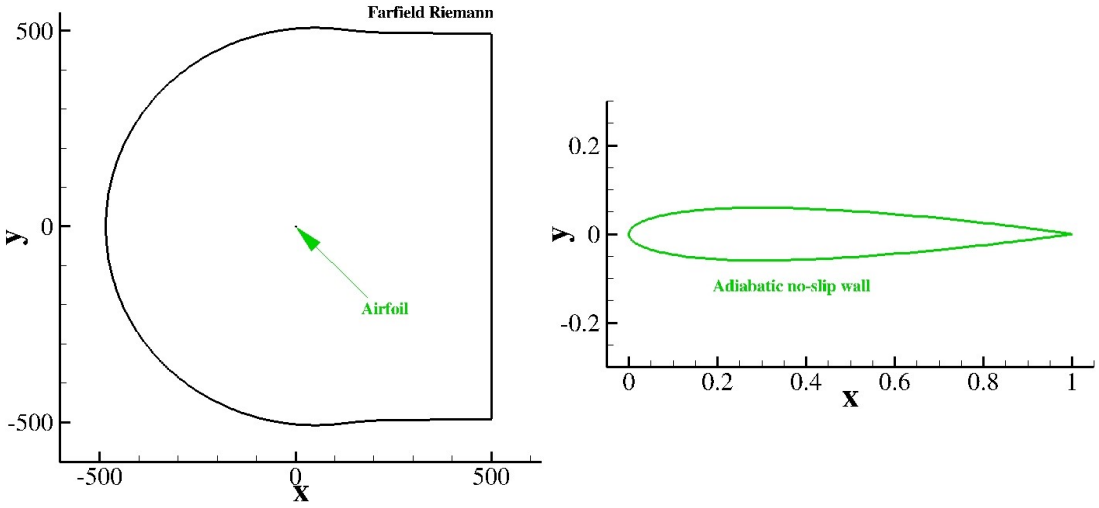

Figure 3.5: Domain and boundary conditions according to [18] for the calculation of the two-dimensional flow over the NACA0012 airfoil

extended to the wake. Finally, table 3.3 summarizes quantitative information about each grid.

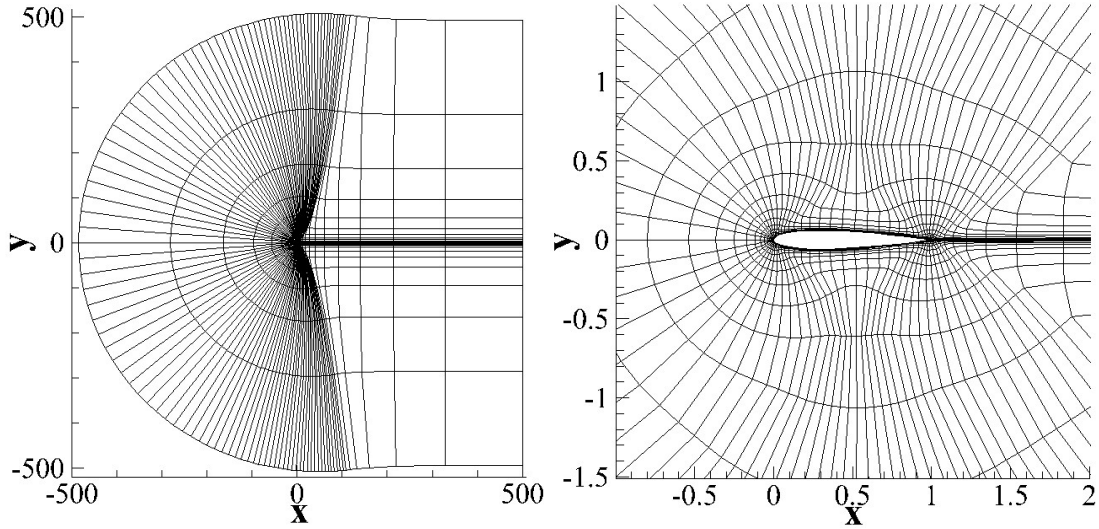

Figure 3.6: Illustration of the coarsest grids ($r_i = 16$) of grid set N. Two-dimensional flow over the NACA0012 airfoil.

Table 3.3: Total number of cells N_{cells}, number of boundary faces in the solid surface N_{wall} and grid refinement ratio r_i of the grids used. Two dimensional viscous flow over the NACA0012 airfoil.

	Set N			
Grid	r_i	N_{cells}	N_{wall}	y^+_{max}
1	1.00	917 504	1024	0.065
2	2.00	229 376	512	0.135
3	4.00	57 344	256	0.288
4	8.00	14 336	128	0.678
5	16.0	3 584	64	Undefined

3.1.2 Inviscid flow

The second set of test cases feature the 2D inviscid flow in a channel over a bump for three flow regimes (subsonic, transonic and supersonic). This test case is found in the open literature and it has been used to test pressure-based solvers [4, 9]. Although outside the typical speed range for maritime and offshore applications, this case was selected to test the robustness and accuracy of ReFRESCO in the presence of sharp variations of flow properties, like the Mach number in shocks. Out of the testing goal is the complex aspects of viscous flow, like shock-boundary layer interactions.

Domain's geometrical characteristics and boundary conditions depend on the incoming flow Mach number. The subsonic and transonic regimes share the same domain and boundary conditions and are depicted in the top picture of figure 3.7, while in the bottom illustration is clear a reduction in the bump height for the supersonic regime, as well as, the different boundary conditions.

Both domains extend for three meters in the streamwise direction and have one meter of total height. A symmetrical bump, of one meter in length, is centred around the origin of the x-axis at the lower side of the domains. The only difference for the different flow regimes is that for the supersonic case the bump height is reduced from 0.1m, in the subsonic and transonic cases, to 0.04m.

For the subsonic and transonic flow conditions the density, velocity and temperature are prescribed at the inlet while the pressure level is defined at the outlet. The velocity is prescribed in order to get a Mach number of 0.5 for the subsonic flow and 0.675 for the transonic. For the supersonic condition the flow is supersonic in the entirety of the domain, so the hyperbolic nature of the Euler equations require the prescription of all variables at the inlet and the extrapolation of all quantities at the outlet[1]. The upper and lower boundaries are adiabatic slip walls.

Two grids sets were used for this test case. However, their distinction is only justified due to the geometrical variations of the bump itself since they have equal number of cells and present the same topology. Table 3.4 presents quantitative information about each grid applicable to both sets. Each set is composed of 9 geometrically similar non-uniformly spaced Cartesian grids and the sparsest grid of each set is illustrated in figure 3.8. The sparsest grids for this study $(4 \leq r_i \leq 44)$ have cell densities close to the grids often found in literature for this test case. Such lower grid resolution may lead to unreliable data for convergence properties estimation. This fact, in turn, explains the need to add finer grids for the sets of this test case. However, in the supersonic test case, there were still some doubts about the extrapolations performed with data obtained from grids with $1 \leq r_i \leq 4$ and so extra grids were generated reaching a refinement level of $r_i = 0.5$.

[1] Considering the outlet boundary to remain orthogonal to the lower boundary.

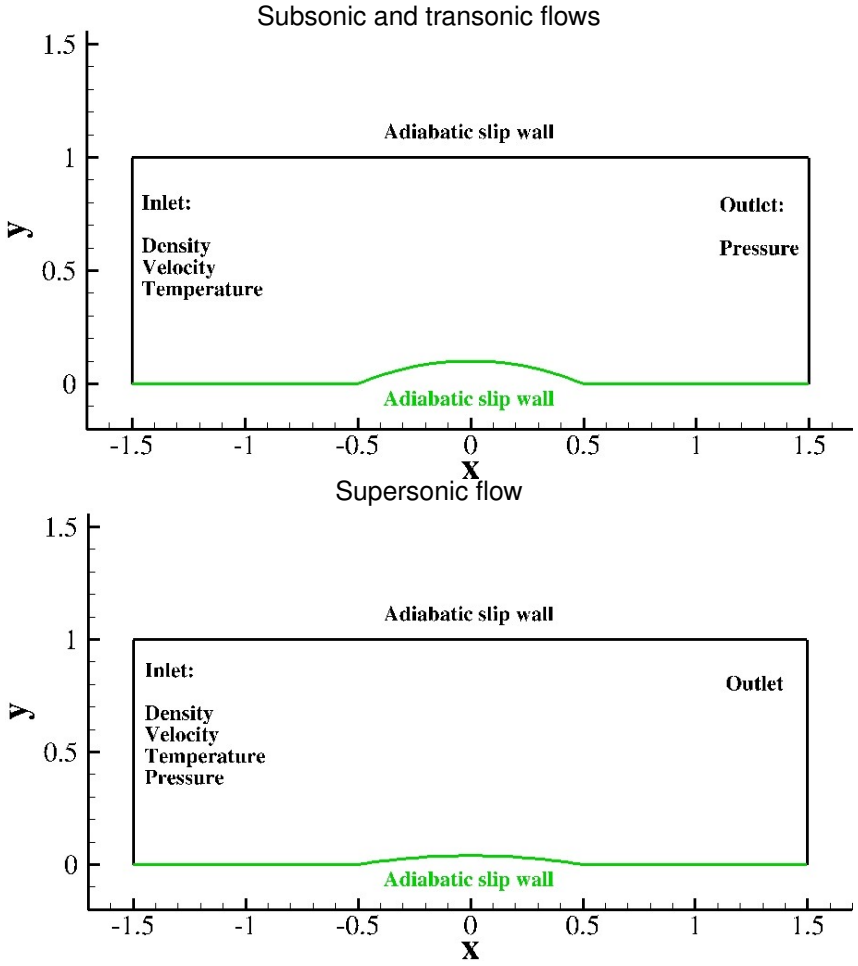

Figure 3.7: Domain and boundary conditions for a two-dimensional inviscid fluid flow over a circular-arc (bump).

Table 3.4: Total number of cells N_{cells}, number of boundary faces in the bump N_{wall} and grid refinement ratio r_i of the grids used. Two dimensional inviscid flow over a bump.

	Subsonic and Transonic			Supersonic		
Grid	r_i	N_{cells}	N_{wall}	r_i	N_{cells}	N_{wall}
a	-	-	-	0.5	1 982 464	2 816
b	-	-	-	0.645	1 192 464	2 184
c	-	-	-	0.861	669 124	1 636
1	1.0	495 616	1 408	1.0	495 616	1 408
2	1.375	262 144	1 024	1.375	262 144	1 024
3	2.0	123 904	704	2.0	123 904	704
4	2.75	65 536	512	2.75	65 536	512
5	4.0	30 976	352	4.0	30 976	352
6	5.5	16 384	256	5.5	16 384	256
7	11	4 096	128	11	4 096	128
8	22	1 024	64	22	1 024	64
9	44	256	32	44	256	32

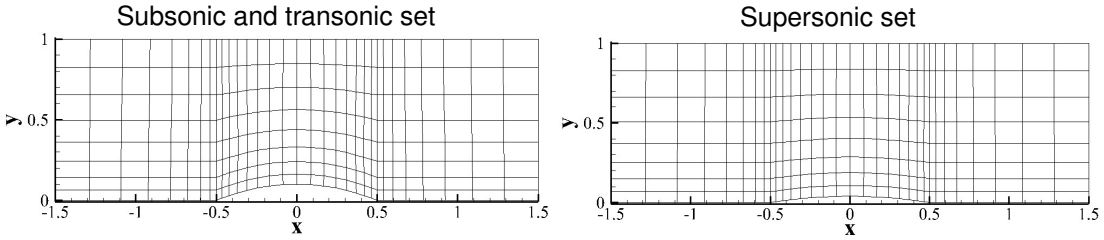

Figure 3.8: Illustration of the coarsest grids ($r_i = 44$) of subsonic and transonic grid set and supersonic grid set. Two-dimensional inviscid flow over a bump.

3.2 Order of grid convergence

The discretization properties of the solver were determined through numerical uncertainty and observed order of grid convergence. Those procedures are thoroughly explained in [20] and a brief description will be here given.

In summary, for a problem with no exact solution, which includes most practical applications involving fluid dynamics equations, an estimation of the discretization error is required to evaluate the accuracy of the solver. The Richardson extrapolation is considered for that purpose, where it is assumed that iterative errors and round-off errors are negligible for the complete numerical error, thus discretization errors are the main contributor for the latter. Since all calculations were done in double-precision format, the round-off error contribution is irrelevant. Furthermore, if the non-linear problem iterative convergence criteria (see sub-section 2.2.3) is respected, the same can be assumed for this component of the numerical error. As a result, an estimate for the discretization error ϵ_ϕ, of a flow quantity ϕ, is given from:

$$\epsilon_\phi = \phi_i - \phi_o = a h_i^p \tag{3.4}$$

where a is a constant, p is the observed order of grid convergence, ϕ_i and ϕ_o are both flow quantity values in a grid with the typical cell size h_i and the estimate of the exact solution, respectively.

However, equation 3.4 is only suitable for a set of data obtained in the asymptotic range and monotonic behaviour are present. To improve the applicability of the error estimation process, three other error estimators were considered. Their expressions are written in equations 3.5. The values of a, a_1, a_2, ϕ_o, and p, are computed in the least-squares sense and among the fitted lines produced, the one with minimum standard deviation from the data set is chosen. The two-terms estimator (eq. 3.5c) is only applicable to non-monotonically convergent data and, naturally, the value of p is not defined.

$$\epsilon_\phi = \phi_i - \phi_o = a h_i \ , \tag{3.5a}$$

$$\epsilon_\phi = \phi_i - \phi_o = a h_i^2 \tag{3.5b}$$

and

$$\epsilon_\phi = \phi_i - \phi_o = a_1 h_i + a_2 h_i^2 \ . \tag{3.5c}$$

The final objective of these procedures is to define the uncertainty levels of a set of data for a desired quantity. The uncertainty values are defined so that the exact solution is contained within an interval with 95% confidence. Besides considering the computed error's estimate, uncertainty values also take into account a safety factor, which can either be 1.25, if monotonic data is used, or 3 for all the other data behaviours.

When presenting the results for the grid convergence studies of chosen flow quantities, the fits performed with eq. 3.4 are referenced by the value obtained for p with 2 significant figures, while the fixed order expressions (eq. 3.5a and 3.5b) results are identified with only 1 significant figure. Lastly, if equation 3.5c represents the best fit for the input data set, it will appear referenced as "$ah + bh^2$" in the legend of the plots.

Chapter 4

Results and discussion

4.1 Quantities of interest

4.1.1 Viscous flow

The quantities of interest analysed under the viscous flows test case conditions are:

- Skin friction coefficient C_f, both its distribution and its value at a specific location, along the wall boundaries;

$$C_f = \frac{\tau_w}{\frac{1}{2}\rho_{ref}U_{ref}^2} = \frac{\tau_w}{\frac{1}{2}P_{ref}\gamma M^2} \,, \tag{4.1}$$

  where τ_w is the shear stress on the wall.

- Pressure coefficient C_p distribution for the wall boundaries of viscous bump and NACA0012 case studies;

$$C_p = \frac{P - P_{ref}}{\frac{1}{2}\rho_{ref}U_{ref}^2} \,. \tag{4.2}$$

- Pressure drag coefficient C_{D_p};

$$C_{D_p} = \frac{F_p}{\frac{1}{2}\rho_{ref}U_{ref}^2 L_{ref}} \,, \tag{4.3}$$

  where F_p is the resulting pressure force component aligned with the incoming flow direction.

- Viscous drag coefficient C_{D_v};

$$C_{D_v} = \frac{1}{L_{ref}} \int_0^{L_{ref}} C_f \mathrm{d}x \,, \tag{4.4}$$

- Total drag coefficient C_D;

$$C_D = C_{D_p}. + C_{D_v} \,. \tag{4.5}$$

- Lift coefficient C_L;

$$C_L = \frac{L}{\frac{1}{2}\rho_{ref}U_{ref}^2 L_{ref}} \,, \tag{4.6}$$

where L is the resulting force component orthogonal to the incoming flow direction.

Additionally, all integrals are calculated with a second-order mid point rule; and a third-order cubic interpolation is used for the values C_f and C_p at specific locations.

4.1.2 Inviscid flow

Whereas to study the numerical properties of the solver in the inviscid flow over a bump test cases, the following quantities were selected:

- Mach number Ma distribution along the bottom and top walls of the inviscid bump test case; equation 2.1.3.
- Force coefficients C_X and C_Y on the bottom wall;

$$C_X = \frac{\int_{-1.5}^{1.5} P dy}{\frac{1}{2}\rho_{ref} U_{ref}^2 L_{ref}} \tag{4.7}$$

$$C_Y = \frac{\int_{-1.5}^{1.5} P dx}{\frac{1}{2}\rho_{ref} U_{ref}^2 L_{ref}} \ . \tag{4.8}$$

- Change of entropy Δs in the bottom wall;

$$\frac{\Delta s}{R} = \frac{\gamma}{\gamma - 1} \ln\left(\frac{T}{T_{ref}}\right) - \ln\left(\frac{P}{P_{ref}}\right) \ . \tag{4.9}$$

- Stagnation temperature T_o along the bottom wall; equation 2.11a.
- Stagnation pressure P_o along the bottom wall; equation 2.11b.
- Primitive flow variables, temperature T and pressure P, along the bottom wall;

As in the previous sub-section, all integrals are calculated with a second-order mid point rule; and a third-order cubic interpolation is used to determine the values of Ma, Δs, T_o, P_o, T and P at specific locations.

4.2 Iterative convergence

Initial condition

The simulations in this thesis were not always performed with the same initial conditions. In total, three options were used: copy the undisturbed flow variables to the complete domain; interpolate the solution at the cells centre using an iteratively converged solution obtained in a different grid; and using an iteratively converged solution obtained in the same grid, but with a different discretization scheme.

All figures illustrating the iterative convergence history of ReFRESCO simulations in this section are with respect to the first or second option.

4.2.1 Viscous flow

2D Zero Pressure Gradient Flat Plate

Figure 4.1 illustrates the iterative convergence history of the L_∞ normalized residual norm of all equations: x and y momentum balance, pressure-correction (continuity), energy equation, and turbulence model equation; as a function of the non-linear iteration counter. Additionally, each plot also contains the changes of dimensionless dependent variables between two consecutive iterations and, on the right axis, the number of iterations performed on the linear system that solves the pressure-correction equation (see sub-section 2.2.3). The simulations hereby presented were carried out on the grids with $r_i = 1$ and $r_i = 2$ of sets N and IM and were all started with an uniform flow solution. The relaxations used of these simulations are summarized in table 4.1.

The number of non-linear iterations to satisfy the convergence criteria increases from around 5×10^4 to approximately 10^5 with grid refinement. This increase is in part attributed to the fact of the solver being segregated and the influence of the chosen under-relaxation parameters.

Figure 4.1 shows that the iterative evolution of the solution on both sets is not equal. The IM grids show noisier convergences than the N grids, especially in the pressure-correction equation (black colour lines) and energy equation (green colour lines). Another aspect that should be highlighted is the different behaviour of the linear solver in the solution of the pressure-correction equation. For the IM grids shown in figure 4.1 the maximum number of linear iterations was reached more often than for the simulations performed with the N grids. Lastly, figure 4.1 also shows that the convergence level reached by the non-linear normalized residuals is similar to that of the changes between iterations.

Table 4.1: Under-relaxation parameters of the simulations performed in the grids with $r_i = 1.$ and $r_i = 2.$ of the sets N and IM. Two-dimensional flow over a flat plate.

		Momentum		ΔP		Energy		$\tilde{\nu}$	
Set	Grid	α_i	α_e	α_i	α_e	α_i	α_e	α_i	α_e
N	1	0.975	0.04	1.	0.04	0.975	0.04	0.975	0.06
N	2	0.975	0.06	1.	0.06	0.975	0.06	0.975	0.06
IM	1	0.975	0.04	1.	0.04	0.975	0.04	0.975	0.06
IM	2	0.975	0.06	1.	0.06	0.975	0.06	0.975	0.08

The origin of the irregular convergence behaviour for the IM grids was assessed following two hypotheses:

1. The convergence level of the linear system of equations was insufficient;

2. The normalization factors were changing during the simulation run. This is explained by the fact that the normalization procedure is performed with the main diagonal value a_P. Since, by definition, the L_∞ norm is the maximum residual value, which is not guaranteed to be at the same location

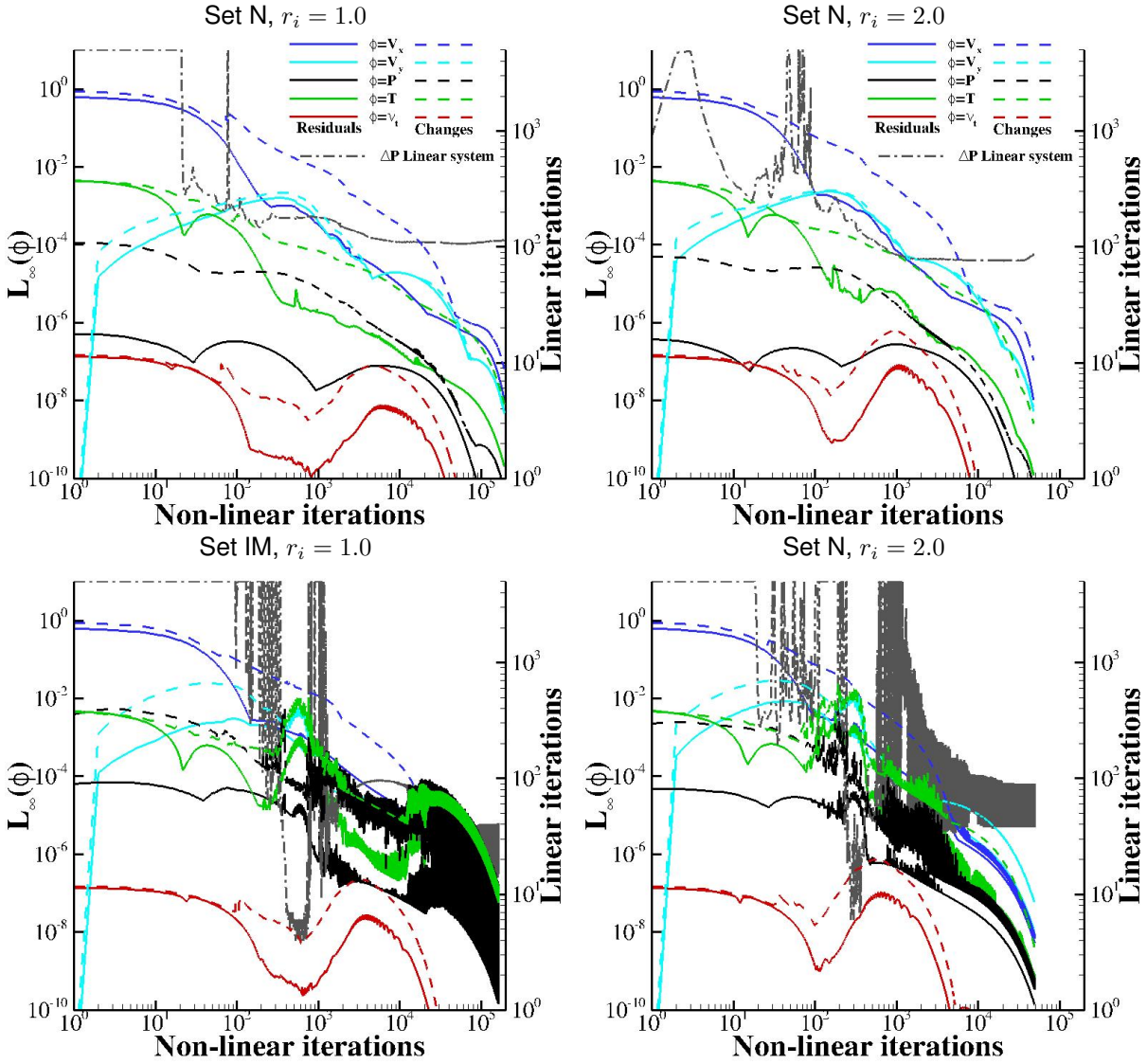

Figure 4.1: Illustration of the iterative convergence (L_∞ norm) in the grids with $r_i = 1.0$ and $r_i = 2.0$ of the sets N and IM. Two-dimensional flow over a flat plate.

in the domain until the end of the simulation, the value of a_P may change to represent the cell with higher residual in a specific iteration.

For the first assumption, two simulations were performed in the grid with $r_i = 2$ of set IM using the relaxation parameters presented in table 4.2. One simulation ran with the bJacobi preconditioner, while the other used the direct solver with complete LU factorization (SuperLU) as the pressure correction preconditioner. The iterative convergence results are presented in figure 4.2.

The number of non-linear iterations to satisfy convergence is smaller than those presented in figure 4.1 for the same grid, from 50 000 to 25 000. However, the simulations in figure 4.2 were started from a previously converged solution interpolated from a coarser grid (grid with $r_i = 8.0$). As a result, higher values of the under-relaxation factors were permitted since the solution is more stable in the earlier stages of convergence.

Nonetheless, figure 4.2 showcases the impact of the pressure-correction preconditioner since the

non-linear iterative convergence with the SuperLU preconditioner is perfectly smooth, whereas bJacobi results exhibit oscillations and insufficient convergence of the linear system of equations. However, the simulation with SuperLU was approximately 1.4 times more time consuming than the one with the bJacobi.

The L_2 norm of the residuals and variable changes, for the same simulation illustrated in figure 4.2 with the bJacobi preconditioner is presented in figure 4.3. Although some oscillations were smoothed out, there are still some irregularities at similar stages of the iterative convergence history. This indicates that the oscillations are mainly coming from lack of convergence in the linear system of equations.

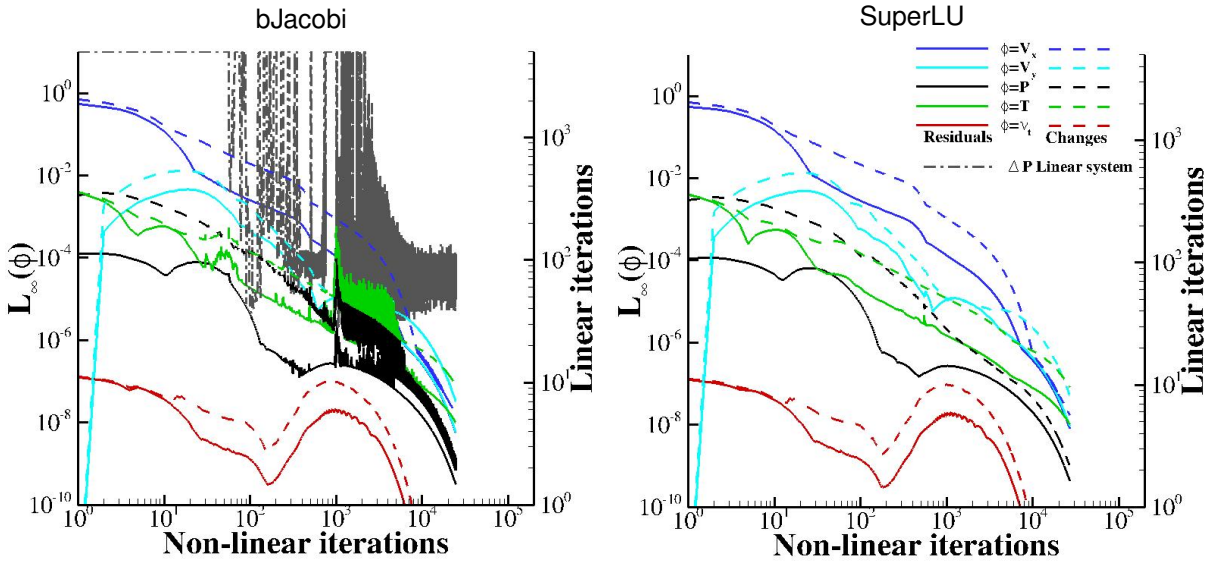

Figure 4.2: Illustration of the iterative convergence (L_∞ norm) in the grid with $r_i = 2.0$ of set IM using two different preconditioners in the pressure correction equation, block Jacobi (bJacobi) and the direct solver SuperLU. Two-dimensional flow over a flat plate.

Table 4.2: Under-relaxation parameters of the simulations performed in the grid with $r_i = 2.$ of the set IM using two different preconditioners in the pressure correction equation, block Jacobi (bJacobi) and the direct solver SuperLU. Two-dimensional flow over a flat plate.

ΔP	Momentum		ΔP		Energy		$\tilde{\nu}$	
Preconditioner	α_i	α_e	α_i	α_e	α_i	α_e	α_i	α_e
bJacobi	0.875	0.2	1.	0.1	0.875	0.3	0.875	0.3
SuperLU	0.875	0.175	1.	0.0875	0.875	0.275	0.875	0.275

2D Bump-in-channel

In the viscous bump test case, iterative convergence was generally harder to achieve due to the decrease of the rate of convergence throughout the residual evolution history. Figure 4.4 depicts the L_∞ residual norm in the grid with $r_i = 4$ of set N as a function of the non-linear iteration counter. The changes of dimensionless variables between two consecutive iterations are also reflected in the same plot.

The simulation presented in figure 4.4 was run with the complete LU factorization for the linear system

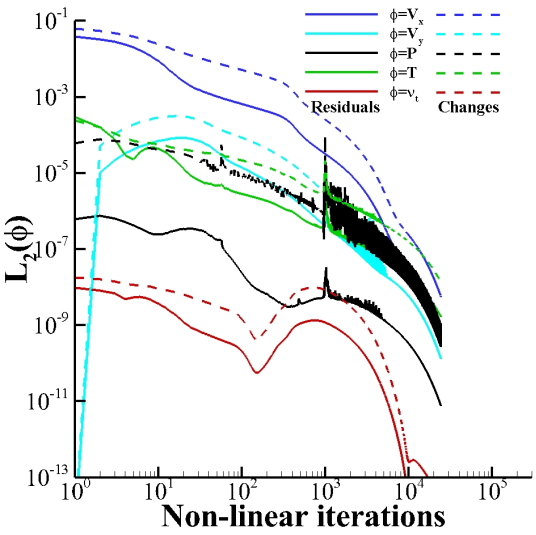

Figure 4.3: Illustration of the iterative convergence (L_2 norm) in the grid with $r_i = 2.$ of set IM using the block Jacobi preconditioner in the pressure correction equation. Two-dimensional flow over a flat plate.

of the pressure-correction equation. The noisier convergence of the energy equation is bellow the convergence criteria so it is of little concern. However, the spotlight of this analysis is on the decrease of rate of convergence with the simulation time. For example, for the figure shown, around 13 000 iterations of the non-linear system were required to drop the residuals from 10^6 to 10^7 while, from that point until the specified convergence criteria, 50 000 more were necessary. Here, the changes between each consecutive iteration are, generally, one order of magnitude higher than the residual, thus enhancing the sensitivity of the solution to the simulation time. The origin of the degradation of the iterative rate is attributed to the fact that the near-wall cell size is replicated in the wake, where the eddy viscosity is non-zero. Diffusive effects scale with the inverse square of the cell spacing multiplied by the eddy viscosity $\left(\propto \mu_t/(\Delta {x_i}^2)\right)$, hence these terms become very large with the small near-wall distances used in this test case (table 3.2). Nonetheless, all grids for this test case were successfully iteratively converged, either using the GMRES for the convergence of the linear system of equations or the SuperLU preconditioner.

The increasingly lower rates of convergence with respect to the residual evolution obtained for this test case motivated the following experiment: compare an insufficiently converged solution with a solution that respected the convergence criteria defined in sub-section 2.2.3. More precisely, one solution was taken from a point in convergence history whereby the highest value of L_∞ norm was, approximately, 4×10^{-6}.

So, figure 4.5 showcases the skin friction coefficient C_f and pressure coefficient C_p distributions along the plate+bump on the finest grid of set N. The red line represents the insufficiently converged solution (NConv.) and the green-coloured line the converged solution (Conv.).

It is evident that the lack of iterative convergence resulted in an overestimation of C_f. Furthermore, the disparities in C_p between the two solutions are also noticeable. Nonetheless, the results of C_p seem to be less sensible to iterative convergence criteria than the ones of C_f.

To further emphasize the importance of reducing the iterative error, figure 4.6 presents the order of grid convergence studies of an integral quantity, C_L, and a surface quantity, C_f at $x \approx 0.63m$, using the

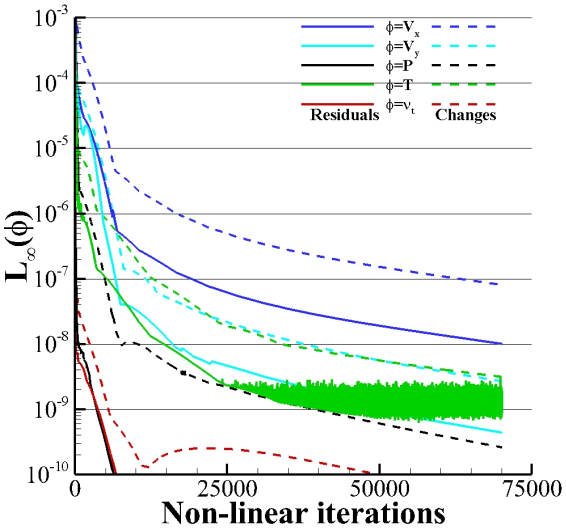

Figure 4.4: Illustration of the iterative convergence (L_∞ norm) in the grid with $r_i = 4.0$ of set N. Two-dimensional viscous flow over a bump.

two solutions of ReFRESCO. The estimation was performed with the data from the four finest grids, using grid doubling, and the uncertainty bars are showcased for the finest grid of the set. Only the simulation on the finest grid was insufficiently converged and the solutions on the remaining grids respected the iterative convergence criteria.

From the results in 4.6, it is clear the negative impact of the finest grid solution in the data set since the uncertainty bars encompass values between 10%, and 5.7%, of the finest grid solution for C_L, and C_f, respectively. Furthermore, the red colour fitted lines do not intersect any grid solution. The first-order grid convergence estimated for the insufficiently converged data set indicates that equation 3.5a (which assumes a set value for "p" equal to 1) ensured the best fit to the solution of the four finest grids. This is an example where reporting of the computed order of grid convergence should be done carefully.

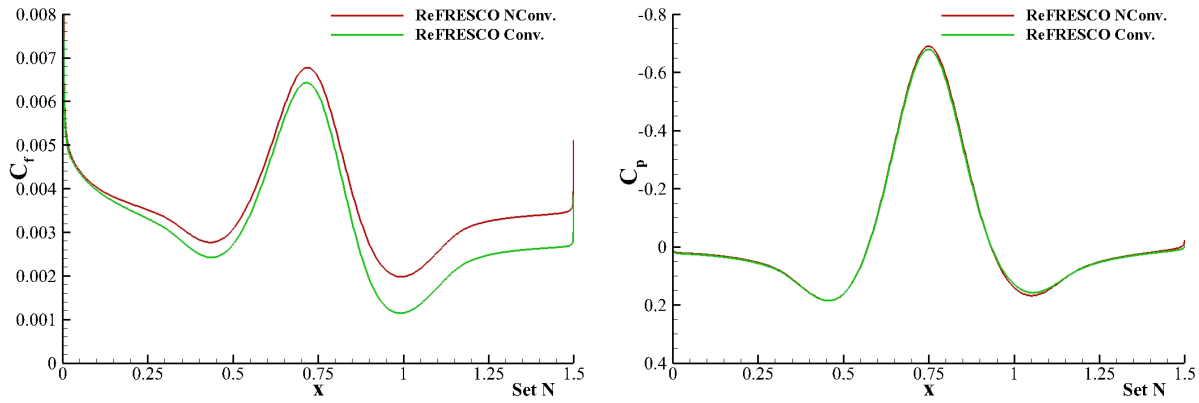

Figure 4.5: Skin friction coefficient C_f and pressure coefficient C_p along the solid surface obtained with in the finest grid of set N. NConv. represents a simulation stopped when the highest value of L_∞ was, approximately, 4×10^{-6}; Conv. is for a simulation iteratively converged until 10^{-8} of the L_∞ norm. Two-dimensional viscous flow over a bump.

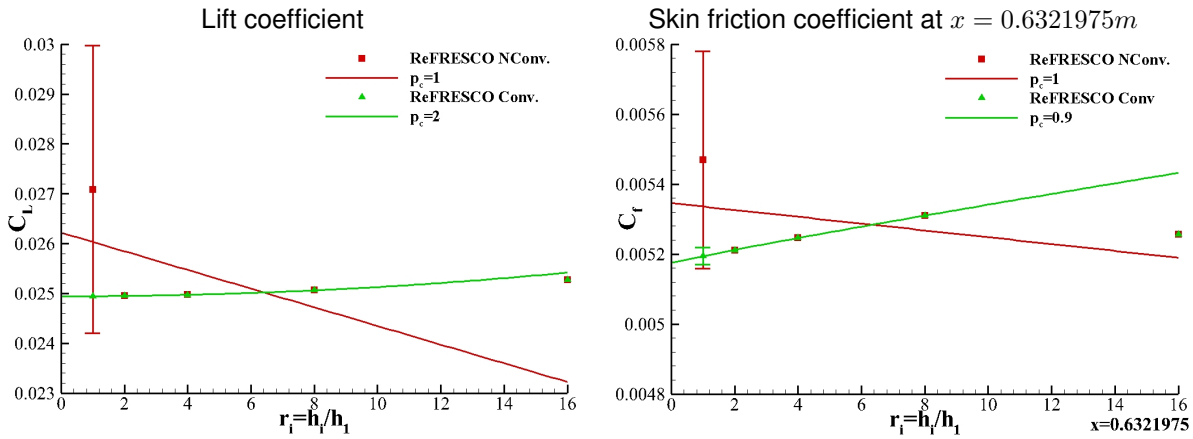

Figure 4.6: Order of grid convergence studies for the lift coefficient C_L and skin friction coefficient C_f at $x = 0.970084m$ as a function of the grid refinement ratio r_i obtained with ReFRESCO. NConv. represents a simulation stopped when the highest value of L_∞ was, approximately, 4×10^{-6}; Conv. is for a simulation iteratively converged until 10^{-8} of the L_∞ norm. Two-dimensional viscous flow over a bump.

2D NACA0012 Airfoil

Figure 4.7 illustrates the L_∞ norm of the residual evolution as a function of the non-linear counter, as well as the changes of dimensionless variables and the number of iterations in the linear system of the pressure correction equation. The simulation was performed in the grid with $r_i = 4.0$ of set N with the block Jacobi preconditioner and initial solution is a uniform flow field.

The same trends are observed between the residual evolution on the NACA0012 and the ones in the viscous flow over a bump test case. Here, the near-wall clustering of cells also extends to the wake of the foil, hindering the non-linear convergence rate considerably with simulation time. For instance, around 40 000 non-linear iterations were required to drop the normalized residual to 10^{-7}, but 150 000 more were necessary to meet the specified convergence criteria. As a result, due to time constraints, the solutions for this test were taken from a point in convergence history where the normalized residual was 10^{-7}. At this point, only the changes in the solution of the momentum-balance equation in x are higher than the new stopping criteria.

Convergence of the linear-system to solve the pressure-correction equation is achieved throughout most of the non-linear problem solution, with exception to the early stages that are a consequence of the initialization procedure. The spontaneous spikes, followed by high-gradient drops, present in figure 4.7, are a consequence of adjusting the under-relaxation parameters during the simulation run. In table 4.3 only the last set of relaxations are presented.

It should be mentioned that simulations in the grid with $r_i = 16.0$ were unsuccessfully iteratively converged due to divergence of the solution in the earlier stages. Several attempts were done, either with varying relaxation parameters, initialization procedures and preconditioners, but always with the same end-result.

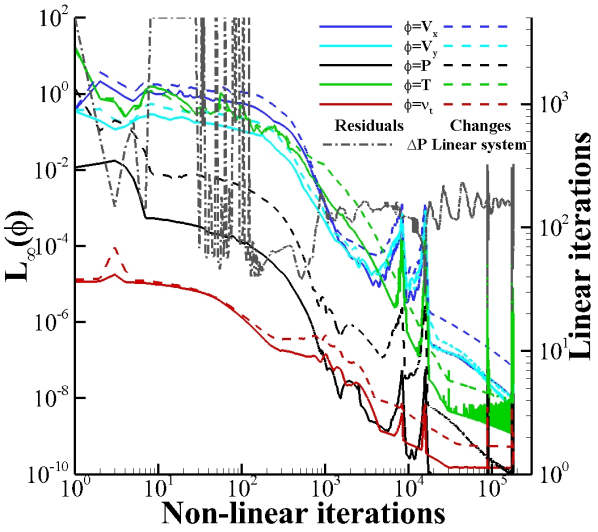

Figure 4.7: Illustration of the iterative convergence (L_∞ norm) in the grid with $r_i = 4.0$ of set N. Two-dimensional flow over the NACA0012 airfoil.

Table 4.3: Under-relaxation parameters of the simulations performed in the grid with $r_i = 4.0$ of set N . Two-dimensional flow over the NACA0012 airfoil.

		Momentum		ΔP		Energy		$\tilde{\nu}$	
Set	Grid	α_i	α_e	α_i	α_e	α_i	α_e	α_i	α_e
N	3	0.85	0.1	1.	0.05	0.85	0.05	0.85	0.05

4.2.2 Inviscid flow

On the inviscid bump test cases, the influence of the undisturbed flow Mach number on the robustness of ReFRESCO will be analysed. As a result, figure 4.8 illustrates the convergence of the L_∞ norm of the normalized residuals with respect to the non-linear counter for the subsonic, transonic, and supersonic flow conditions. The simulations hereby illustrated were performed in the grids with $r_i = 5.5$ using a Fromm scheme with the harmonic limiter in the convective terms of momentum and energy equations. Additionally, the linear system of equations was solved with GMRES plus the block Jacobi preconditioner.

Similar iterative rate was obtained with the subsonic and supersonic test cases, whereas the transonic conditions are more demanding on the solver iterative convergence. However, smoother convergence behaviour was obtained in the transonic and subsonic conditions. The more irregular convergence of the supersonic test case is most likely a consequence of the larger explicit under-relaxation values selected for that case, which are presented in table 4.4. Nonetheless, the convergence rates obtained with ReFRESCO for the transonic and supersonic flow regimes are in line to the ones reported in [4].

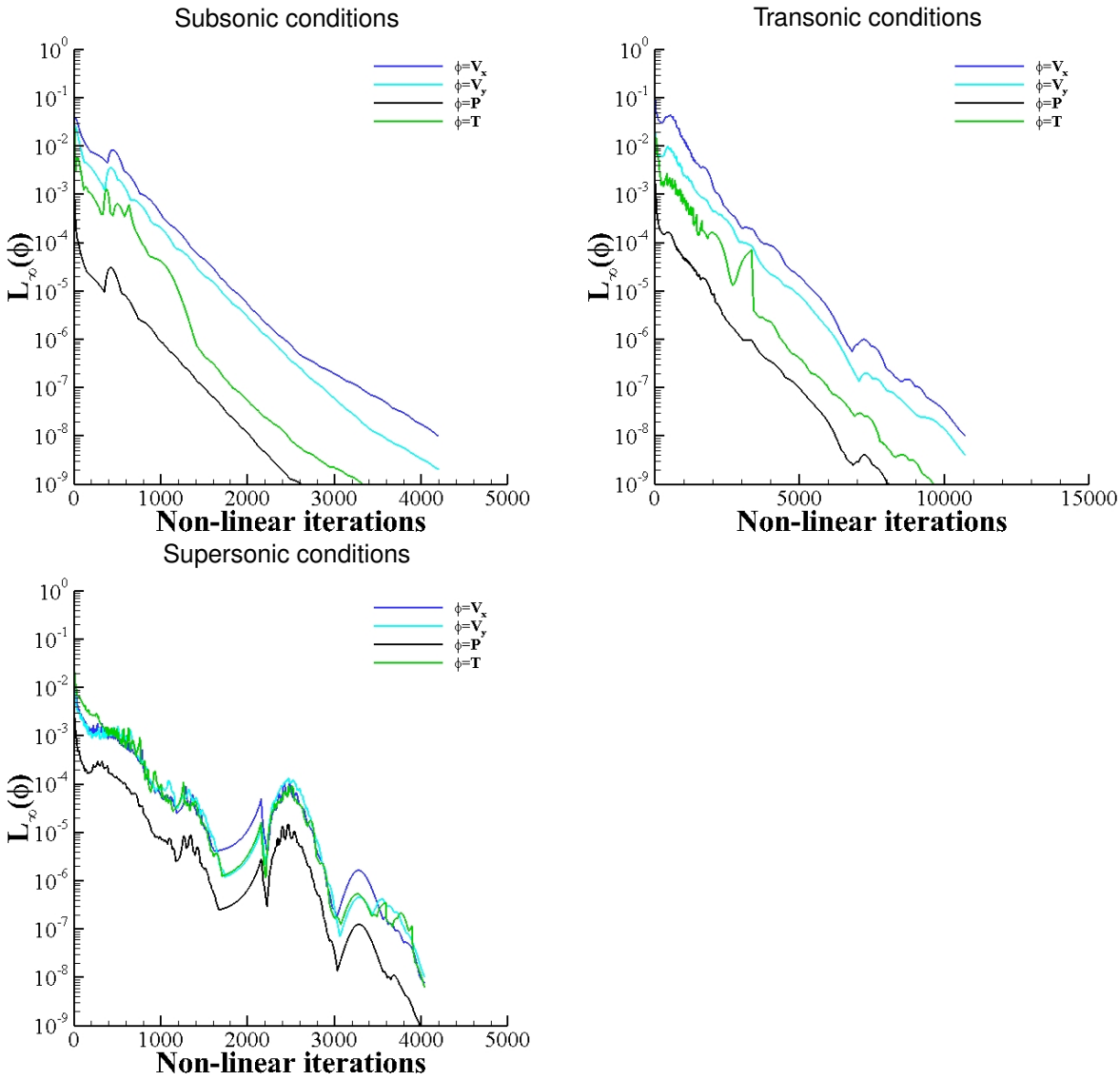

Figure 4.8: Illustration of the iterative convergence (L_∞ norm) in the grid with $r_i = 5.5$ for subsonic, transonic and supersonic conditions. Two-dimensional inviscid flow over a bump.

Table 4.4: Under-relaxation parameters of the simulations performed in the grid with $r_i = 5.5$ for subsonic, transonic and supersonic conditions. Two-dimensional inviscid flow over a bump.

	Momentum		ΔP		Energy	
Regime	α_i	α_e	α_i	α_e	α_i	α_e
Subsonic	0.85	0.10	1.	0.05	0.85	0.05
Transonic	0.85	0.10	1.	0.05	0.85	0.05
Supersonic	0.95	0.35	1.	0.175	0.95	0.175

4.3 Grid convergence studies

4.3.1 Viscous flow

The grid convergence properties were assessed for the quantities of interest referred in sub-section 4.1.1. By nature the results from these studies are dependent on the number of grids used and their

density. To assess this dependence, four different alternatives for the estimation of observed order of grid convergence were chosen:

1. Data from the 5 finest grids of the set, generally with $1 \leq r_i \leq 4$, identified as p_a;
2. Data from 3 grids using grid doubling, i.e. $r_i = 1$, $r_i = 2$, and $r_i = 4$, referred as p_b;
3. Data from 4 grids using grid doubling, i.e. $r_i = 1$, $r_i = 2$, $r_i = 4$ and $r_i = 8$, mentioned as p_c;
4. Data from 5 grids using grid doubling, i.e. $r_i = 1$, $r_i = 2$, and $r_i = 4$, $r_i = 8$ and $r_i = 16$ (p_d).

2D Zero Pressure Gradient Flat Plate

Before presenting the results for the grid convergence studies in the flat plate test case conditions, it should be mentioned that the iterative convergence criteria for the grids with $r_i \leq 2$ was lowered to 10^{-9} and the linear convergence criteria for the pressure-correction equation to 10^{-3}. These adjustments were required in order to minimize the contribution of the iterative error in the total numerical error of the simulations.

The results of grid convergence studies to the drag coefficient C_D and the skin friction coefficient C_f at $x = 0.970084m$ are depicted in figures 4.9 and 4.10, respectively. Both quantities were analysed in the grid sets N and IM. The lines included in the plots represent the best fit, as proposed in [20], to each discrete data set input. However, the estimated uncertainty bar corresponds only to the fit performed for the 5 finest grids (p_a).

The results for the two quantities are consistent between each grid set, which means that the uncertainty bars of the finest grids overlap. Additionally, they also showcase the deviation of the solutions obtained in coarser grids from the fitted lines based on fine grids results. This is further quantified in figure 4.9 by the deterioration of the estimated order of grid convergence if the coarsest grid $r_i = 16$ is included (p_d). Both sets extrapolate the solution for a cell size zero to, approximately, the same value if the grid with $r_i = 16$ is not included in the estimation. The error constant, a, is slightly larger for the IM set than for the set N. Lastly, while the value of p is the same between both sets when evaluating locally C_f, set IM shows lower order of grid convergence for the integral quantity C_D than set N.

2D Bump-in-channel

The set of grids in the viscous bump test case features grids with a fixed refinment ratio of 2. As a result, only the three alternatives for the estimate of the observed order of grid convergence p were studied, p_b, p_c and p_d (see beginning of this sub-section).

Figure 4.11 presents the three alternative estimates of p for C_f and C_p at 20 selected locations on the plate+bump surface. The symbols at null values of p indicate that the best fit to the data is obtained with the two terms expansion (eq. 3.5c).

The two plots suggest the following trends:

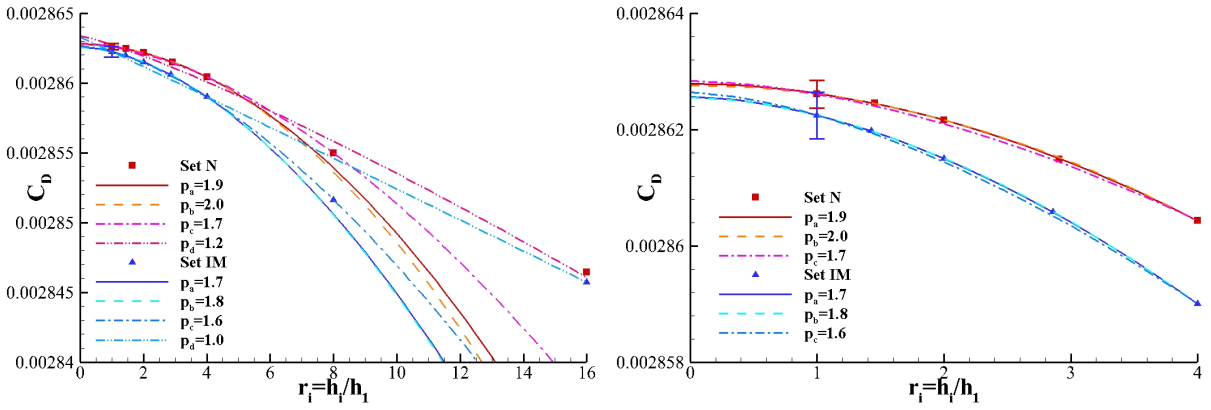

Figure 4.9: Friction drag coefficient C_D as a function of the grid refinement ratio r_i for the N and IM grid sets. p_a is obtained from the 5 finest grids $1 \leq r_i \leq 4$; p_b is obtained from the 3 grids with $r_i = 1$, $r_i = 2$ and $r_i = 4$; p_c is obtained from the 4 grids with $r_i = 1$, $r_i = 2$,$r_i = 4$ and $r_i = 8$; p_d is obtained from the 5 grids with $r_i = 1$, $r_i = 2$,$r_i = 4$, $r_i = 8$ and $r_i = 16$. Two-dimensional flow over a flat plate.

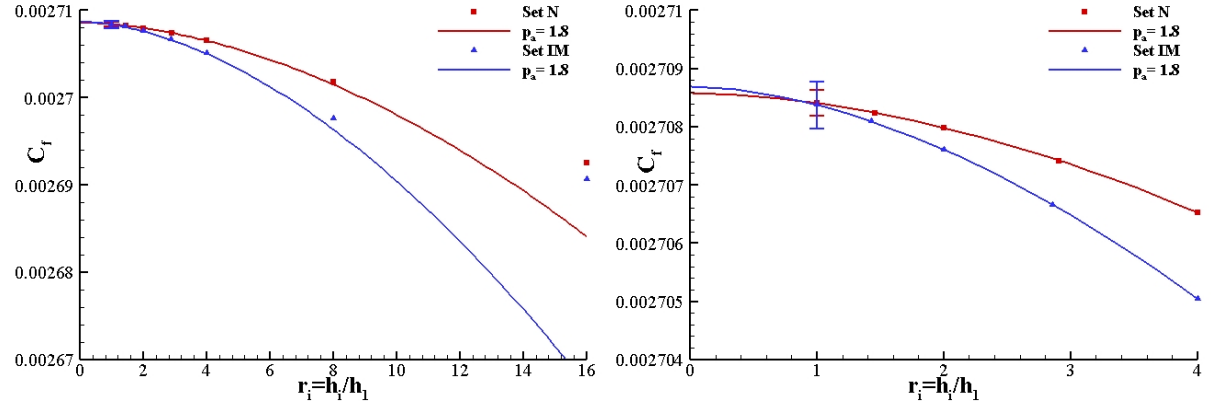

Figure 4.10: Skin friction coefficient C_f at $0.970084m$ away from the leading edge of the plate as a function of the grid refinement ratio r_i for N and IM grid sets. p_a is obtained from the 5 finest grids $1 \leq r_i \leq 4$. Two-dimensional flow over a flat plate.

- The best fit for the solutions at the leading edge for C_p are obtained with the two terms expansions. Whereas, the same estimator is used for the results of C_f in the grids with $1 \leq r_i \leq 8$ at the trailing edge.
- The estimated values of p for C_f show more scatter than the ones for C_p. Not only that, but the estimated order of grid convergence is generally higher for the pressure coefficient.
- Unexpectedly, the inclusion of the coarsest grid solution does not always deteriorate the estimate of p.

The grid convergence histories for C_f and C_p at 3 selected locations are depicted in figure 4.12 for the three alternative estimates of p. One point is close to the leading edge ($x = 0.075m$), the other is located at the bump's peak ($x = 0.75m$) and the third one is close to the trialing edge ($x = 1.35m$). The uncertainty bars correspond to the lines fitted to the solution of the grids with $1 \leq r_i \leq 4$.

The three fits of each plot estimate similar exact solutions. Despite some fits being obtained with the alternative expressions in eq. 3.5, most of the data for C_p in the four finest grids exhibit monotonic convergence.

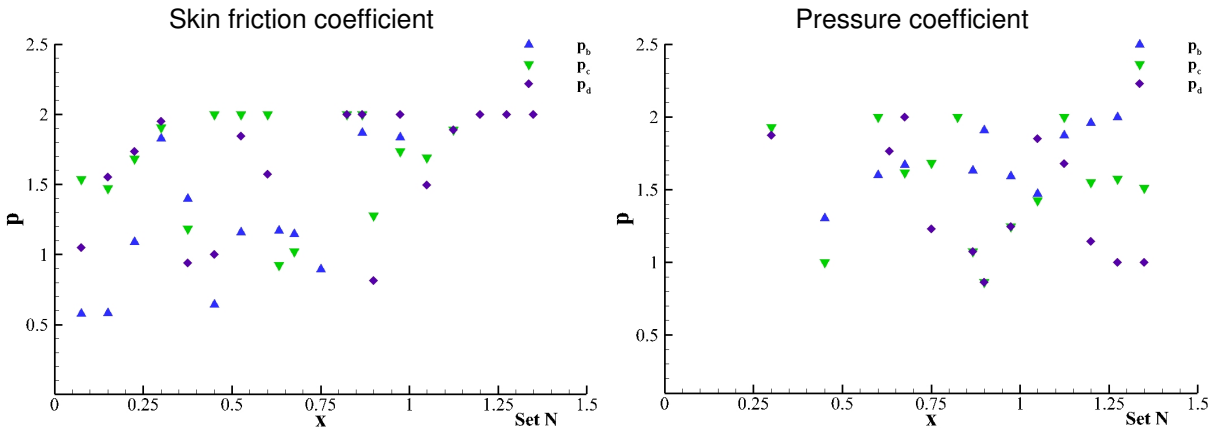

Figure 4.11: Observed order of grid convergence of skin friction coefficient C_f (on the left) and pressure coefficient C_p (on the right). The solutions were taken for 20 different locations along the solid surface. p_b is obtained from the 3 grids with $r_i = 1$, $r_i = 2$ and $r_i = 4$; p_c is obtained from the 4 grids with $r_i = 1$, $r_i = 2$,$r_i = 4$ and $r_i = 8$; p_d is obtained from the 5 grids with $r_i = 1$, $r_i = 2$,$r_i = 4$, $r_i = 8$ and $r_i = 16$. Two-dimensional viscous flow over a bump.

On the other hand, the same observations do not hold for C_f solutions. At the trialing edge, the data set is not in the asymptotic range. C_f at the bump's peak exhibit monotonic convergence if the solutions form the three finest grid are considered. At a location close to the leading edge there is some scatter of the data in the finest grids, nonetheless the value of p is determined.

However, it should be mentioned that these three locations are close to "problematic" regions for evaluation of C_f: singularities are present at the edges of the solid surface, and a cell face is located at $x = 0.75m$ so there is slight eccentricity with respect to the nearby cell centers. Nevertheless. adding extra grids, like in the flat plate test case, may improve the reliability of the data for these estimations.

2D NACA0012 Airfoil

The error discretization estimation for this test case will be restricted to the lift coefficient and total drag coefficient. Figure 4.13 presents the results of the grid convergence studies for both integral quantities at three different angles of attack: $\alpha = 0^o$, $\alpha = 10^o$ and $\alpha = 15^o$. The fitted lines and estimated order of grid convergence were obtained according to the categories defined in 4.3. However, the uncertainty bars are always with respect to the data set of three most refined grids.

Before addressing the results a few limitations have to be acknowledge for the data set of this test case. Firstly, only solutions in grids with fixed refinement ratio of 2 were used. This can lead to estimations with data set outside the asymptotic range. Secondly, the stopping criteria ($L_\infty \leq 10^{-7}$) may be to loose to neglect the iterative error influence, which is a requirement of the procedure used to access order of grid convergence properties.

Starting with $\alpha = 0^o$, the two terms expression (eq. 3.5c) represents the best fitted lines to the input data set. Furthermore, the estimated extrapolated solution to cell size zero for the lift coefficient does not match the expected solution from potential flow theory, i.e. $C_L = 0$ for a symmetric foil aligned with the flow. Nonetheless, the theoretical value is encompassed in the estimated uncertainty bar of the finest grid. Finally, the error estimation properties yield essentially the same results independently of the

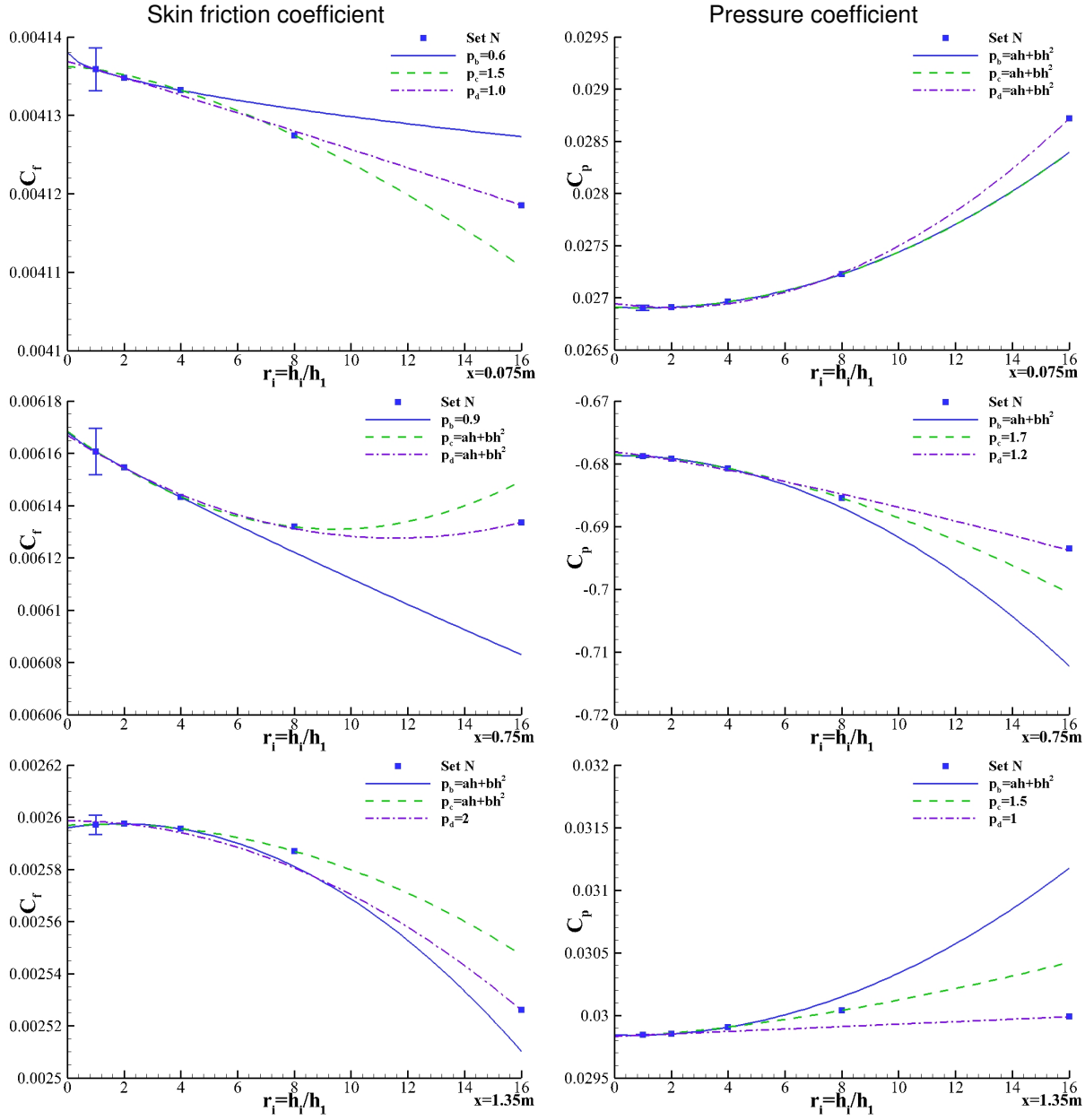

Figure 4.12: Skin friction coefficient C_f (on the left) and pressure coefficient C_p (on the right) at three locations on the solid surface as a function of the grid refinement ratio r_i for the N grid set. p_b is obtained from the 3 grids with $r_i = 1$, $r_i = 2$ and $r_i = 4$; p_c is obtained from the 4 grids with $r_i = 1$, $r_i = 2$,$r_i = 4$ and $r_i = 8$; p_d is obtained from the 5 grids with $r_i = 1$, $r_i = 2$,$r_i = 4$, $r_i = 8$ and $r_i = 16$. Two-dimensional viscous flow over a bump.

number of grids used.

Following with the solutions for $\alpha = 10^o$, the considerations could not be any different from the previous angle of attack. Here, the monotonically-converged data shows almost second-order convergence for C_D and close to first-order convergence for C_L. The estimated orders of grid convergences are larger when using the solutions from the three most refined grids.

Only remains the results with $\alpha = 15^o$, where the observed trends are a bit different from the previous couple of solutions. More precisely, with respect to the influence of the number of grids used in the estimations since monotonic behaviour is not preserved if only the three finest grids are used. However,

when accounting for the solution of the grid with $r_i = 8.0$ the estimated order of grid convergences are 1.5 and 1.1, for C_D and C_L, respectively.

In the end, the angle of attack seems to affect considerably the grid convergence numerical properties of the solver. However, these estimations may be a consequence of iterative errors, particularly the value of p for Cl. Furthermore, extra sufficiently fine grid should be included to avoid using the solution from the grids with $r_i > 4.0$.

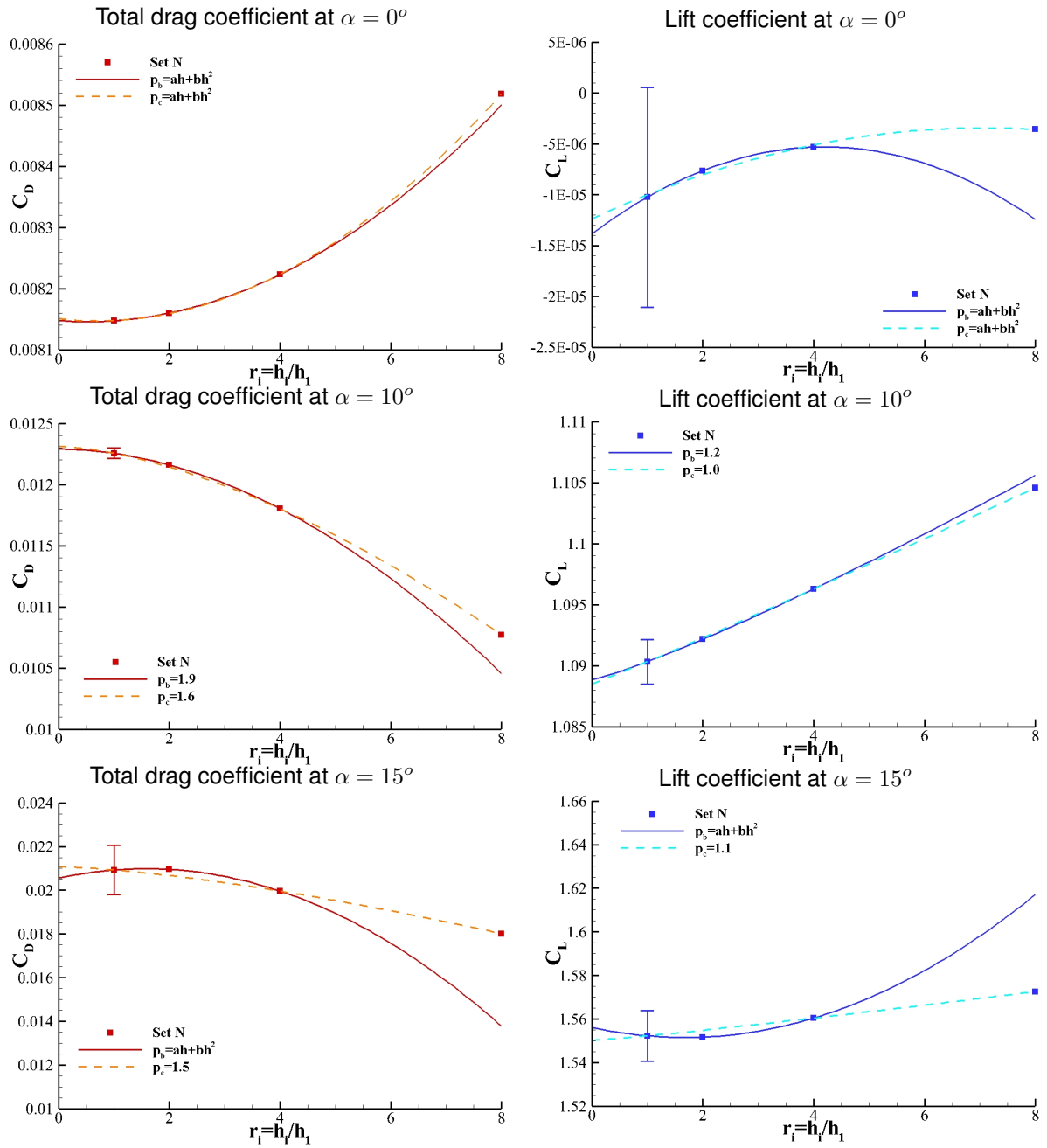

Figure 4.13: Total drag coefficient (on the left side) and lift coefficient (on the right side) as function of the grid refinement ratio r_i for the N set of grids of NACA0012 airfoil at three angle of attacks: $\alpha = 0^o$, $\alpha = 10^o$ and $\alpha = 15^o$. p_b is obtained from the 3 grids with $r_i = 1$, $r_i = 2$ and $r_i = 4$ and p_c is obtained from the 4 grids with $r_i = 1$, $r_i = 2$,$r_i = 4$ and $r_i = 8$. Two-dimensional flow over the NACA0012 airfoil.

4.3.2 Inviscid flow

In the inviscid bump test case, the grid convergence properties are estimated for the three inlet flow regimes: subsonic, transonic and supersonic. The truncated power series expressions explained in 3.2 are fitted to the data of the four most refined grids, being the grids with $1 \leq r_i \leq 2.75$ for subsonic and transonic flows and grids with $0.5 \leq r_i \leq 1$ for the supersonic conditions.

The first set of results present two integral quantities, the force coefficients at the bottom wall, C_X and C_Y. Figure 4.14 illustrates the convergence with grid refinements of the three flow regimes and four convection schemes. The results indicate that the solutions with the four schemes are all consistent since the estimate of the exact solution are in good agreement. C_X extrapolates to zero in the subsonic flow, as it is theoretically expected in a symmetric flow field.

Furthermore, all data set taken to the four finest grids are in the asymptotic range and in general the fits overlap with the solutions obtained in coarser grids ($r_i = 11$, for instance). Exception goes to C_Y in the supersonic case. Here, only the solutions in grids with $r_i < 4$ agree with the fits. These results motivated the use of extra levels of refinement for the supersonic flow, as otherwise monotonic convergence would not be present.

For the subsonic flow, the observed order of grid convergences p seem consistent. The reuslts also show that the use of 10% first-order upwind in the blending is enough to drop p to values close to one. However, there is a drastic reduction in the error constant when compared to fully UP results, evidenced in the slope of the fit.

Concerning the transonic case unexpected values of p are present, like $p = 1.6$ for C_X with the UP scheme. This might suggest the current grid refinement level to be insufficient to establish the order of grid convergence for that scheme. Another strange result is $p = 0.5$ for C_Y with the QUICK scheme. Despite the solutions with the HARM and QUICK schemes being almost coincident, the estimated values of p for the first are considerably higher. This is attributed to very small changes in the solutions the four finest grids.

With fully supersonic flow conditions, the observed order of grid convergence is only possible to establish with the inclusion of the extra refined grids. For instance, the convergence of C_X with the HARM and QUICK schemes only becomes monotonic for grids with $r_i < 3$.

Lastly, it is also evident that the numerical accuracy of the UP solutions in the finest grids is worse than that obtained with the HARM and QUICK schemes with $r_i = 5.5$

Figure 4.15 illustrates the convergence with grid refinement of temperature T and pressure P at one location on the bottom wall, downstream of the second geometric discontinuity. For these local primitive variables, not all fits show monotonic convergence. Nonetheless, most of the trends observed in the force coefficients are also applicable to this set of data. The key difference is related to the consistency of the extrapolation solution across the four schemes. The estimates of the exact temperature for the HARM and QUICK schemes are similar between each other and differ from those obtained with the CDS-10UP and UP schemes.

On the other hand, there is consistency in the extrapolated values for pressure with the four schemes. This fact greatly benefits the convergence properties of the force coefficients as those are only depedent

on one primitive flow variable, pressure.

The final check of the grid convergence properties for this test case are to derived flow quantities such as: Mach Ma, change of entropy Δs, stagnation temperature T_o and stagnation pressure P_o. These quantities are analysed for the same location as in figure 4.15.

Figure 4.16 illustrates the grid convergence properties for Ma and Δs for the four schemes tested across the three flow regimes. The trends observed for the Mach number are similar to those showcased for the temperature. As for T, in the supersonic flow the solutions of the four convection schemes do not extrapolate to the same estimate of the exact solution and the HARM and QUICK schemes yield similar results.

Considering the change in entropy, is it noticeable the deviation from the theoretical exact solution in subsonic flow ($\Delta s = 0$) for the UP scheme results. Since the selected location for the transonic flow is downstream of the bump, the increase in entropy is expected due to the shock. As expected, the values for $\Delta s/R$ for the supersonic flow should be lower than those of the transonic flow. However, the four schemes do not agree on the solution extrapolated to cell size zero. The HARM and QUICK schemes lead to $\Delta s/R < 0$, while the CDS-10UP scheme leads to $\Delta s/R > 0$ and the UP scheme estimates $\Delta s/R = 0$. These differences are explained by the convergence properties of T_o.

For adiabatic flows of an ideal fluid, stagnation temperature should remain constant. However. figure 4.17 showcases that this is not guaranteed for the present numerical simulations. With exception to the supersonic case, the HARM and QUICK schemes extrapolate to the exact solution. The loss of T_o in the supersonic conditions explains the negative values of Δs for the HARM and QUICK schemes.

Lastly, the grid convergence of P_o shows consistent results when extrapolating the solution to cell size zero among the four schemes tested. Again, the supersonic conditions are the exception with consistent results from the HARM and QUICK schemes and discrepancies from the remaining two convection schemes. P_o is depedent on P and Ma. Since the results for P in figure 4.15 are consistent across the four schemes, the trends in P_o are a consequence of the Mach number.

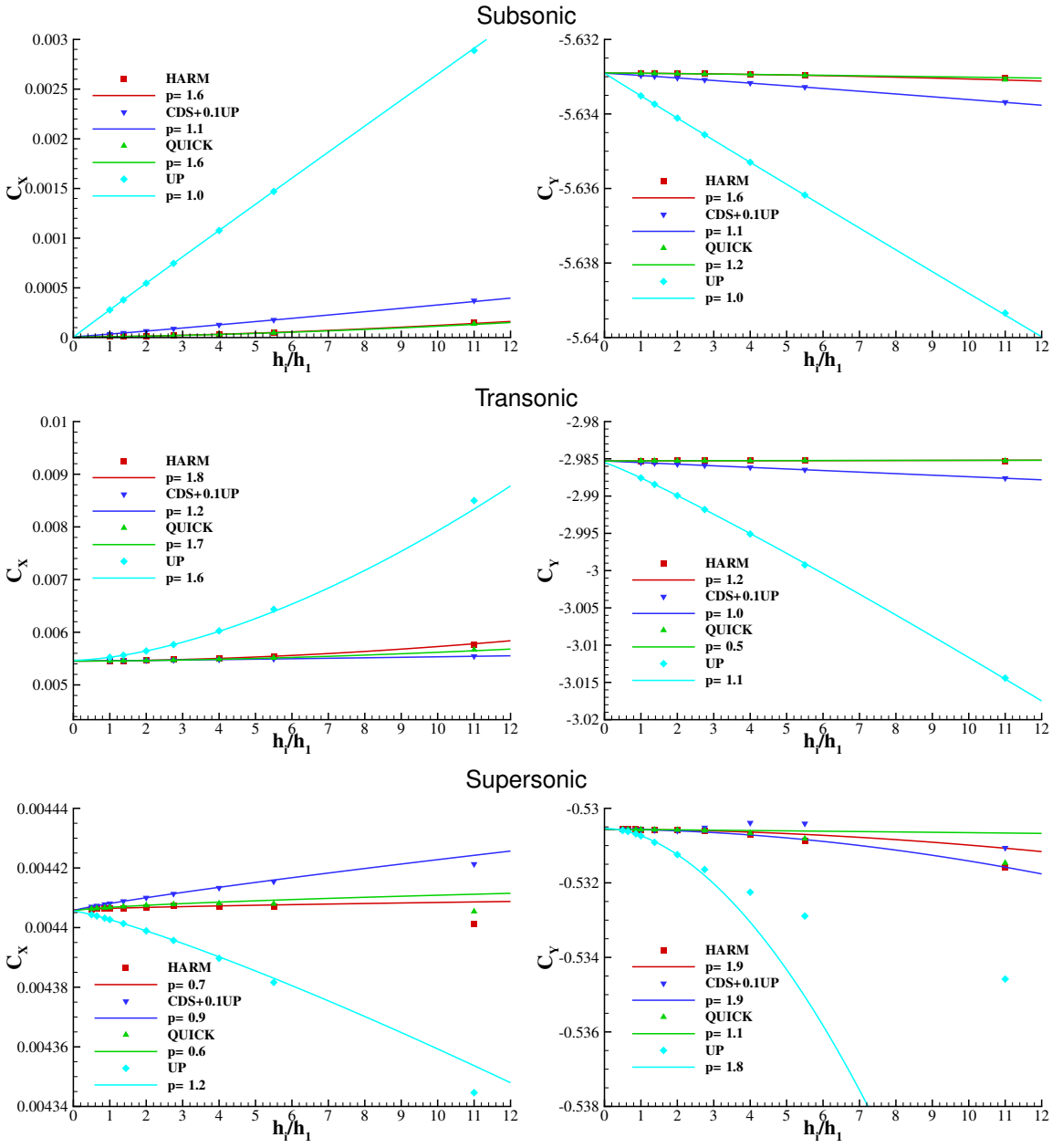

Figure 4.14: Grid convergence of the horizontal C_x and vertical C_y forces coefficients obtained by integration of the pressure on the bottom wall. ReFRESCO results using different convection schemes for the subsonic, transonic and supersonic flows of an inviscid fluid over a bump.

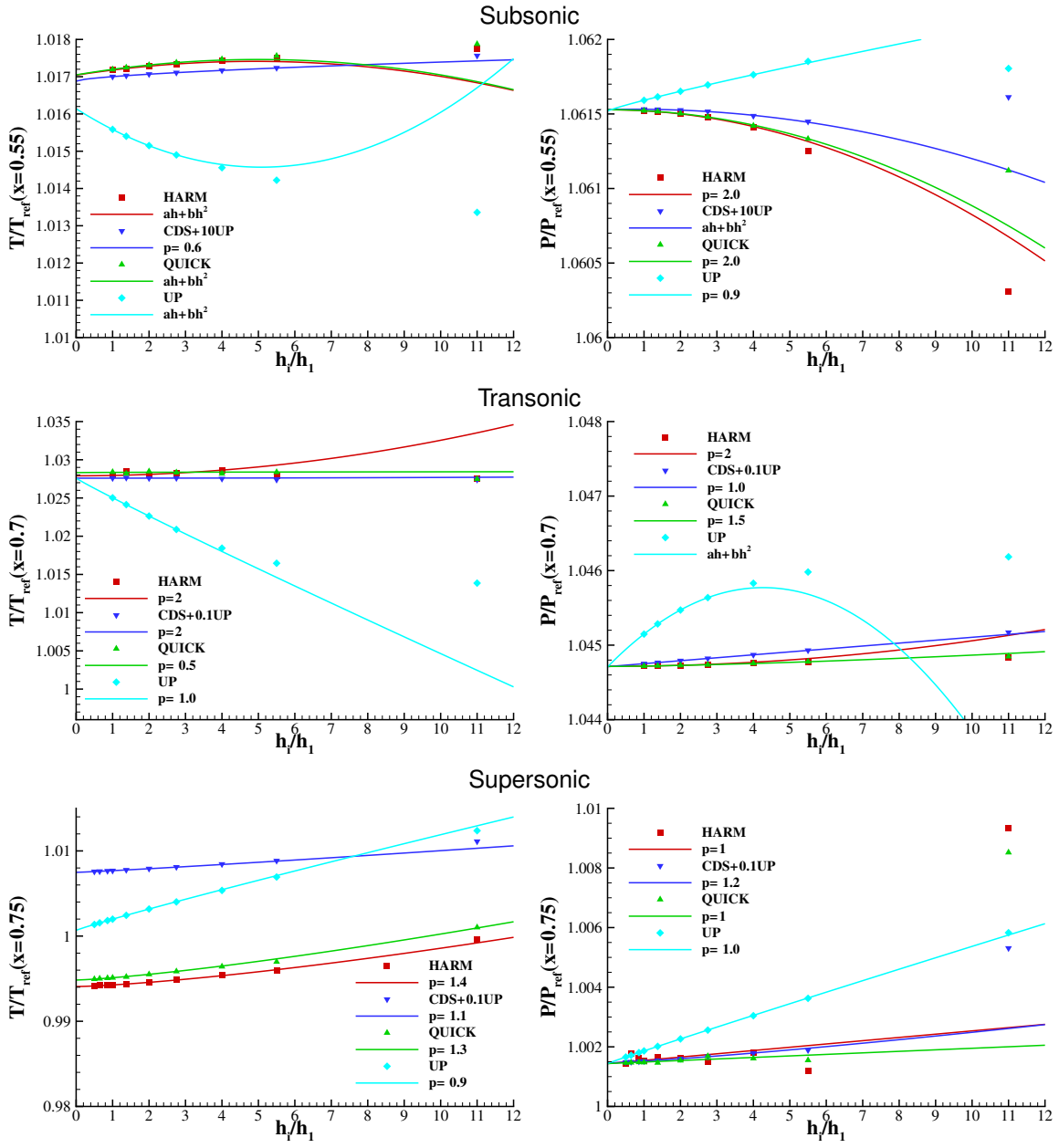

Figure 4.15: Grid convergence of the temperature T and pressure P at one location on the bottom wall. ReFRESCO results using different convection schemes for the subsonic, transonic and supersonic flows of an inviscid fluid over a bump.

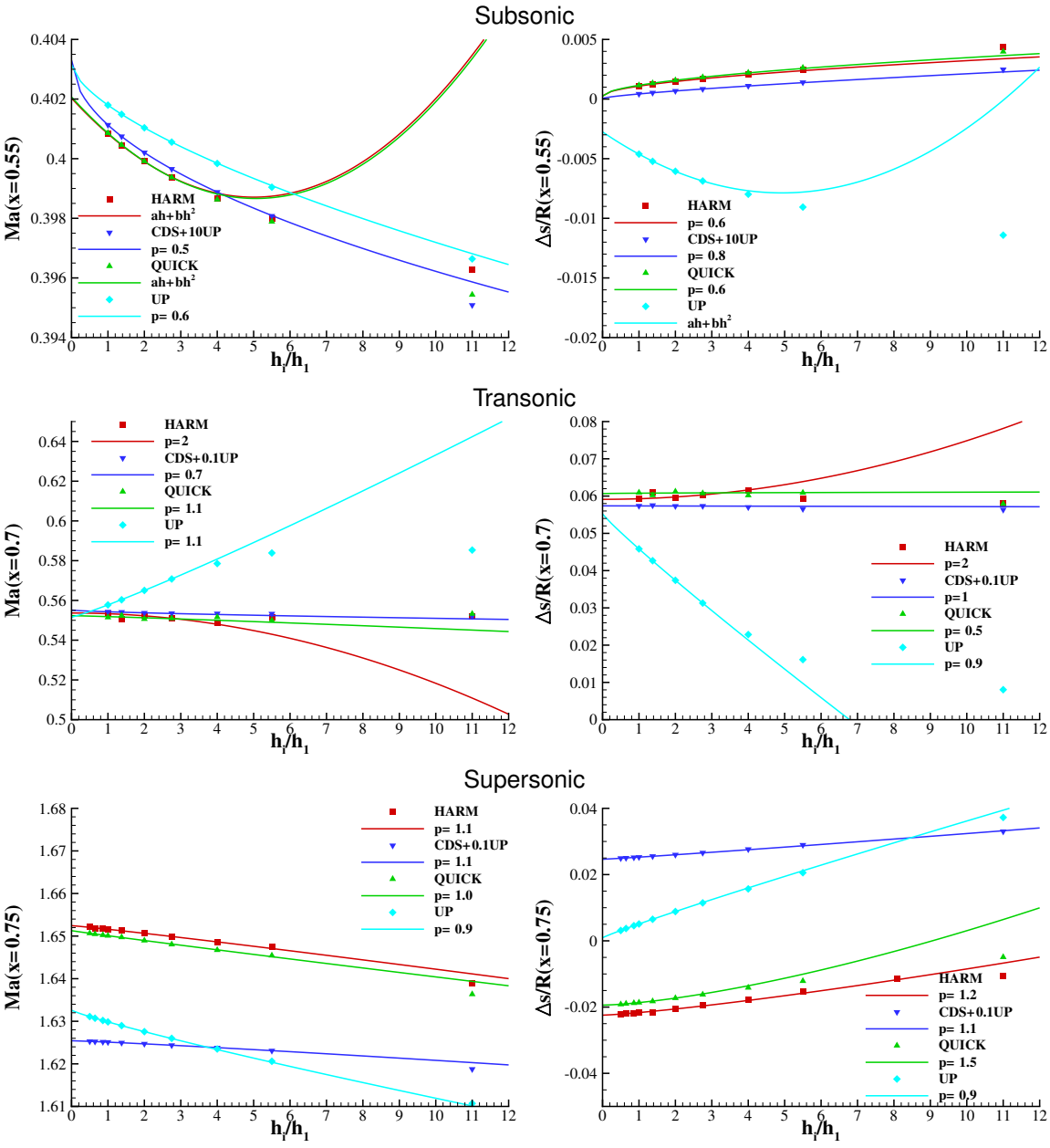

Figure 4.16: Grid convergence of the Mach number Ma and change of entropy Δs at on location on the bottom wall. ReFRESCO results using different convection schemes for the subsonic, transonic and supersonic flows of an inviscid fluid over a bump.

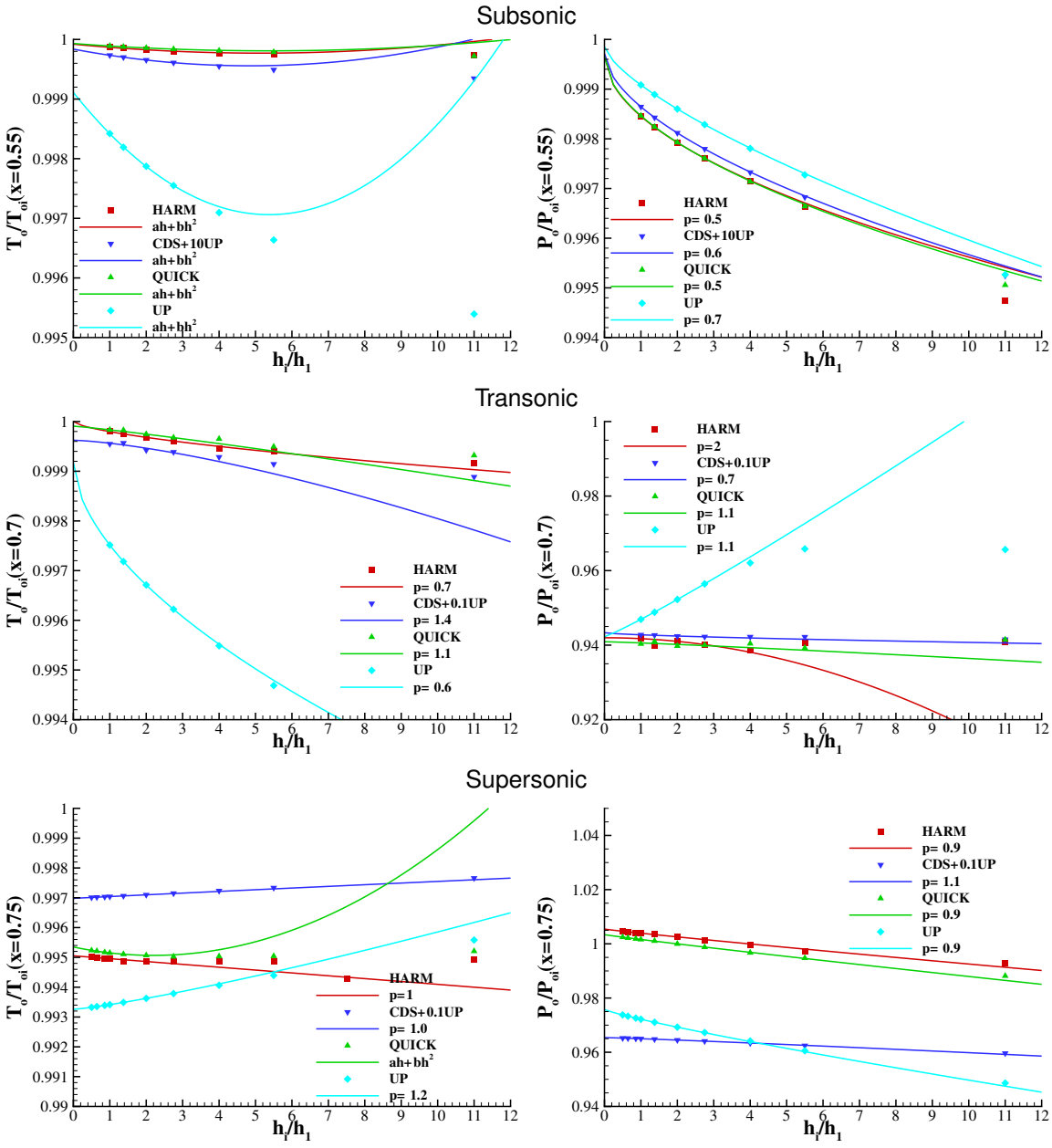

Figure 4.17: Grid convergence of the stagnation temperature T_o and stagnation pressure P_o at one locations on the bottom wall. ReFRESCO results using different convection schemes for the subsonic, transonic and supersonic flows of an inviscid fluid over a bump.

4.4 Code-to-code comparison

This section is reserved to compare results obtained with ReFRESCO with those available in the open literature from other codes. The comparative solutions will include results from: CFL3D flow solver, a cell-centered density-based solver [44]; FUN3D, a vertex-centered density-based solver [45]; digitized data from the works of Gregory, et al. [46]; and experimental data from Ladson, et al. [47]. The results reported by Moukalled, et al. [4], and Pèric, et al. [9], are also replicated here for a side-by-side graphical comparison.

4.4.1 Viscous flow

2D Zero Pressure Gradient Flat Plate

Results from the flat plate test case using ReFRESCO will be compared with the solutions of two other solvers available at [48], CFL3D and FUN3D. The grids available at [49] match the set N of this test case only using grid doubling, i.e., the grids with $r_i = 1.45$ and $r_i = 2.90$ are not present. As a result, the estimates of p will be with respect to p_b, p_c, and p_d, categories defined in sub-section 4.3.1.

Figure 4.18 presents the convergence with grid refinement of C_D for the three solvers. The error bars included in the plots correspond to the fits performed to the three finest grids. To help the comparison between ReFRESCO and the other two solvers, table 4.5 summarizes the estimated values of p, the extrapolated value to a grid with cell size zero C_{D_o}, and the absolute difference of C_{D_o} computed by ReFRESCO relative to the value obtained from the other codes, $|\Delta C_{D_o}|$.

Considering the plots in figure 4.18, there is no overlap of the estimated error bar of ReFRESCO in relation to the other solvers. When using the values from the three finest grids to estimate the extrapolated solution, the largest difference is between ReFRESCO and FUN3D being 0.147% of the solution obtained with ReFRESCO. Additionally, these differences are consistently smaller when comparing ReFRESCO with CFL3D rather than ReFRESCO with the FUN3D solver.

The highest value of p was achieved by ReFRESCO using the three finest grids, and incorporating the coarsest grid in the estimation of the discretization error deteriorates the observed order of convergence. On the other hand, the opposite behaviour is observed for the solutions taken from [48], which is an unexpected result.

Regarding a surface quantity, the first comparison is performed for the grid convergence properties of C_f at $x = 0.970084071m$. Figure 4.19 and table 4.6 present equivalent information to the one showcased in figure 4.18 and table 4.5, respectively. Although, most of the main trends observed in the data of C_D remain accurate for the solutions of C_f, a few changes are worth mentioning:

- The observed order of convergence is always higher for the CFL3D solver, independently of the grids included in the estimation.
- Despite still existing no overlap between the finest grids error bars of ReFRESCO and the other two solvers, the mismatches of the lines are smaller than those obtained in figure 4.18. Those

are reflected in the differences of the extrapolated solutions, $|\Delta Cf_o|$, that are generally lower than those presented for the previous integral quantity.

The distribution of C_f along the plate in the finest grid of set N is represented in figure 4.20 for the three solvers. The right plot of the figure presents the differences between ReFRESCO solution and the solutions of CFL3D (blue colour line) and FUN3D (green colour line). To complement the comparison, the uncertainty values computed from ReFRESCO using data from the three grids with $r_i = 1$, $r_i = 2$, and $r_i = 4$, calculated in selected points throughout the plate were also included.

Visually, the three distributions are identical. However, the right plot shows that the differences between ReFRESCO and the other two solvers are larger than the estimated numerical uncertainty. Generally, the disparities in the skin friction coefficient are around 4×10^{-6}, while the uncertainty levels are close to 2×10^{-7}. Nonetheless, without estimating the numerical uncertainty of the FUN3D and CFL3D solutions, there is no guarantee that the results of ReFRESCO are inconsistent. The latter was not obtained because only the distribution of C_f in the finest grid is given at [48].

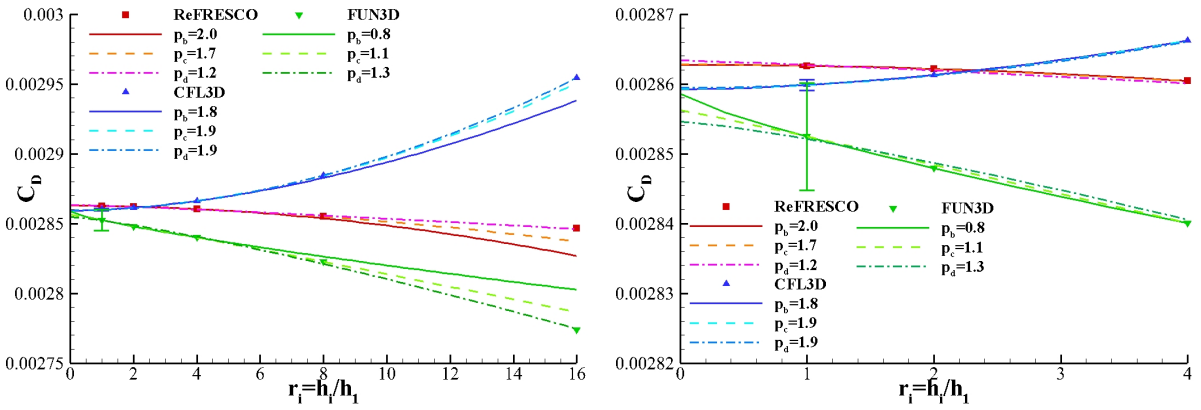

Figure 4.18: Friction drag coefficient C_D as a function of the grid refinement ratio r_i obtained with ReFRESCO, CFL3D and FUN3D in the grids of set N. p_b is obtained from the 3 grids with $r_i = 1$, $r_i = 2$ and $r_i = 4$; p_c is obtained from the 4 grids with $r_i = 1$, $r_i = 2$,$r_i = 4$ and $r_i = 8$; p_d is obtained from the 5 grids with $r_i = 1$, $r_i = 2$,$r_i = 4$, $r_i = 8$ and $r_i = 16$. Two-dimensional flow over a flat plate.

2D Bump-in-channel

The results of the viscous bump test case using ReFRESCO are compared with solutions of CFL3D and FUN3D flows solvers, available at [50].

Figure 4.21 presents the distribution of two flow quantities, C_f and C_p, for the entire solid surface (plate+bump) computed on the finest grid of set N. Additionally, like in figure 4.20, the differences between the solution of the other two solvers and ReFRESCO, and the uncertainty of levels of the latter, were also included.

The skin friction coefficient distributions of the solvers match visually. Only at the edges of the plate, which pose numerical singularities, the differences between the CFL3D and FUN3D with ReFRESCO are considerable. Nonetheless, the quantification of the mismatches averages 5 identical digits. Furthermore, these differences correspond to the numerical uncertainties estimated for ReFRESCO along

Table 4.5: Observed order of grid convergence p, estimated exact solution C_{D_o} and the absolute difference of C_{D_o} computed by ReFRESCO and the one obtained with the other solvers $|\Delta C_{D_o}|$ relative to ReFRESCO solutions, of the friction drag coefficient obtained with ReFRESCO, CFL3D and FUN3D in the N grid set. p_b is obtained from the 3 grids with $r_i = 1$, $r_i = 2$ and $r_i = 4$; p_c is obtained from the 4 grids with $r_i = 1$, $r_i = 2$,$r_i = 4$ and $r_i = 8$; p_d is obtained from the 5 grids with $r_i = 1$, $r_i = 2$,$r_i = 4$,$r_i = 8$ and $r_i = 16$. Two-dimensional flow over a flat plate.

		ReFRESCO	CFL3D	FUN3D
p	b	1.97	1.75	0.80
	c	1.71	1.87	1.05
	d	1.20	1.92	1.25
C_{D_o}	b	2.8628×10^{-3}	2.8592×10^{-3}	2.8586×10^{-3}
	c	2.8628×10^{-3}	2.8593×10^{-3}	2.8562×10^{-3}
	d	2.8634×10^{-3}	2.8594×10^{-3}	2.8546×10^{-3}
$\lvert\Delta C_{f_o}\rvert$	b	-	0.126%	0.147%
	c	-	0.122%	0.231%
	d	-	0.140%	0.308%

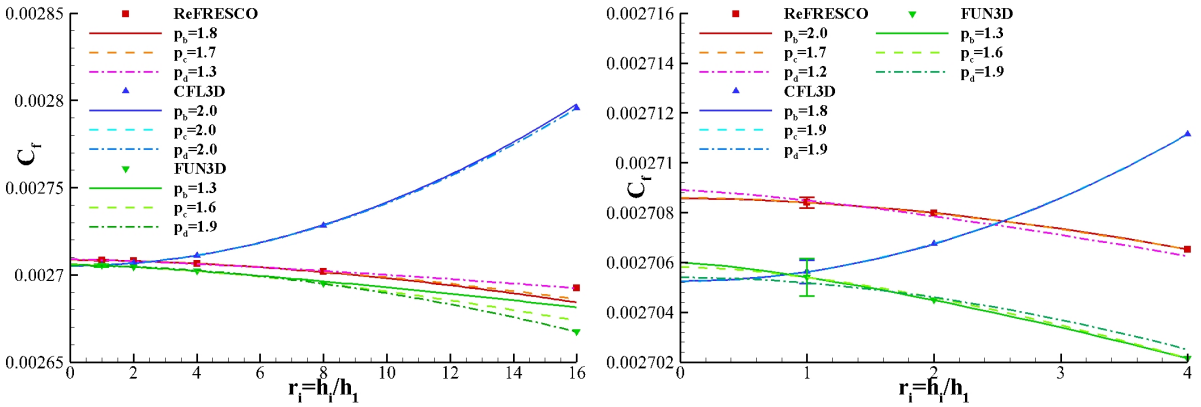

Figure 4.19: Skin friction coefficient C_f at $x = 0.970084m$ as a function of the grid refinement ratio r_i obtained with ReFRESCO, CFL3D and FUN3D in the N grids set. p_b is obtained from the 3 grids with $r_i = 1$, $r_i = 2$ and $r_i = 4$; p_c is obtained from the 4 grids with $r_i = 1$, $r_i = 2$,$r_i = 4$ and $r_i = 8$; p_d is obtained from the 5 grids with $r_i = 1$, $r_i = 2$,$r_i = 4$, $r_i = 8$ and $r_i = 16$. Two-dimensional flow over a flat plate.

the bump. As a result, the solution from ReFRESCO is consistent with the results available in the open literature.

When comparing the pressure coefficients there are graphical disparities. However, those were attributed to distinct reference pressure levels since the computed differences along the solid surface are almost a constant horizontal line. Unfortunately, the set reference pressure defined for the comparative codes was not found, while for the ReFRESCO simulations the outlet pressure of the domain is the reference value (see 3.1.1). Without clarifying this problem, no statement can be made concerning the consistency (or inconsistency) of ReFRESCO results when evaluating the C_p distribution.

As far as grid convergence properties are concerned, the selected integral quantities are: total drag coefficient C_D, lift coefficient C_L, pressure drag coefficient C_{D_v} and viscous drag coefficient C_{D_p}. The reuslts of ReFRESCO are displayed on figure 4.22, together with the solutions available at [50]. Grid convergence studies for C_f, at $x \approx 0.63m$ and $x \approx 0.75m$, is illustrated in figure 4.23. Among the four

Table 4.6: Observed order of grid convergence p, estimated exact solution C_{f_o} and the absolute difference of C_{f_o} computed by ReFRESCO and the one obtained with the other solvers $|\Delta C_{f_o}|$ relative to ReFRESCO solutions, of the skin friction coefficient at $x = 0.970084m$ obtained with ReFRESCO, CFL3D and FUN3D in the N grid set. p_b is obtained from the 3 grids with $r_i = 1$, $r_i = 2$ and $r_i = 4$; p_c is obtained from the 4 grids with $r_i = 1$, $r_i = 2$,$r_i = 4$ and $r_i = 8$; p_d is obtained from the 5 grids with $r_i = 1$, $r_i = 2$,$r_i = 4$,$r_i = 8$ and $r_i = 16$. Two-dimensional flow over a flat plate.

		ReFRESCO	CFL3D	FUN3D
p	b	1.79	1.98	1.34
	c	1.72	1.97	1.56
	d	1.32	1.97	1.86
C_{f_o}	b	2.7086×10^{-3}	2.7052×10^{-3}	2.7060×10^{-3}
	c	2.7086×10^{-3}	2.7052×10^{-3}	2.7058×10^{-3}
	d	2.7089×10^{-3}	2.7052×10^{-3}	2.7054×10^{-3}
$\|\Delta C_{f_o}\|$	b	-	0.126%	0.096%
	c	-	0.126%	0.103%
	d	-	0.137%	0.129%

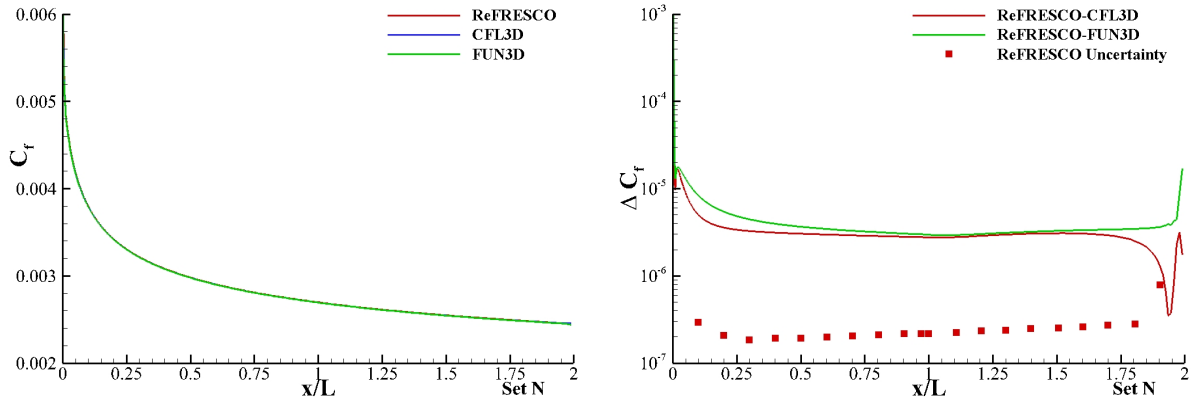

Figure 4.20: Skin friction coefficient C_f along the plate obtained with ReFRESCO, CFL3D and FUN3D in the finest grid of set N. Uncertainty estimates of ReFRESCO are obtained from the 3 grids with $r_i = 1$, $r_i = 2$ and $r_i = 4$. Two-dimensional flow over a flat plate.

categories for assessing the grid convergence properties presented in the beginning of section 4.3, two were chosen for the following set of results, those being p_b and p_c. The fitted lines and uncertainty bars presented in the figures above are with respect to the solutions of the grids with $1 \leq r_i \leq 4$.

The results for C_L are in the asymptotic region, except when using the solutions of ReFRESCO in the 4 most refined grids. The computed solution for a grid with cell size zero of ReFRESCO is also in great agreement with the other solvers as the differences between those are, at maximum, 0.084%, considering the data obtained from the 3 most refined grids. This information is summarized in table 4.7, which contains the computed order of grid convergence, the extrapolated solution and the mismatches between that computed by ReFRESCO and by the other two solvers.

On the other hand, the results for C_D feature mostly data sets outside the asymptotic region. The sensitivity of the drag coefficient to the grids refinement level can be explained by the distribution of C_f. More precisely, the resolution of the numerical singularities located at the leading and trailing edges of the solid surface. As seen in the inviscid bump results, local refinements in that regions greatly affect

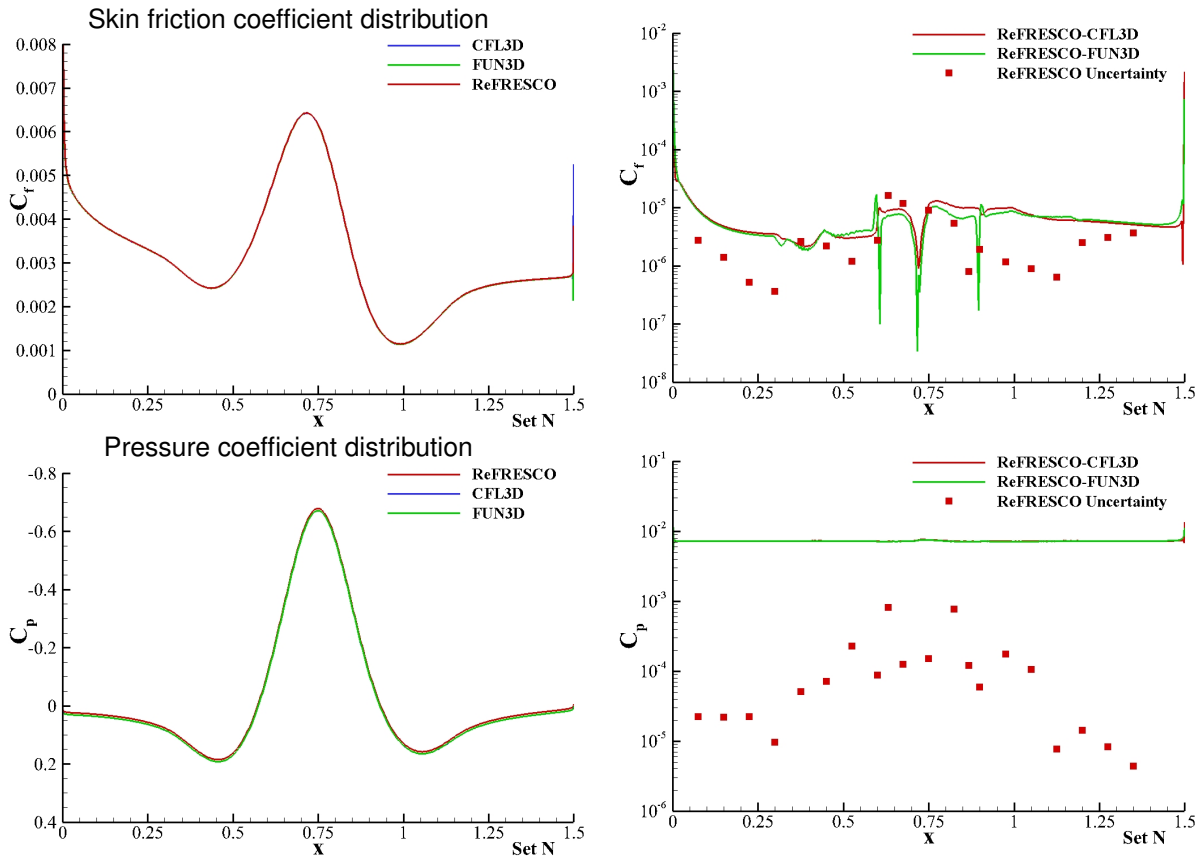

Figure 4.21: Skin friction coefficient C_f and pressure coefficient C_p along the solid surface obtained with ReFRESCO, CFL3D and FUN3D in the finest grid of set N. Uncertainty estimates of ReFRESCO are obtained from the 3 grids with $r_i = 1$, $r_i = 2$ and $r_i = 4$. Two-dimensional viscous flow over a bump.

the resolution of this discontinuities. As a result, reliable estimates of p may require finer grids than the ones present in this set. Nonetheless, the estimated numerical uncertainty is very small (almost indistinguishable from the symbol for the finest grid) and the differences from the extrapolated solution are close to 0.145% when comparing the values obtained from the 3 most refined grids, as evidenced in table 4.8.

The grid convergence studies for two components of C_D, C_{D_v} and C_{D_p}, confirm the the previous observations. The integration of the viscous forces exhibits oscillatory behaviour in the finest grids, while the convergence of the remaining component is smooth. Interestingly, the contribution of C_{D_p} in the total drag coefficient is enough to dissimulate the oscillatory behaviour promoted by C_{D_v}. Nevertheless, the solutions of ReFRESCO are in agreement with those of other codes for these two components as well.

The last results of this test case concern the numerical convergence properties of the skin friction coefficient at two different locations: $x = 0.6321975m$ and $x = 0.75m$. Equivalent information to table 4.7 is presented with respect to the numerical properties of the skin friction in $x = 0.6321975m$ and $x = 0.75m$ on tables 4.9 and 4.10, respectively.

Regarding the consistency of ReFRESCO, the same observations as in the integral quantities can be made. However, these results showcase that Solution Verification exercises are specific to each flow quantity and may vary depending on the location in the domain where the estimations are performed.

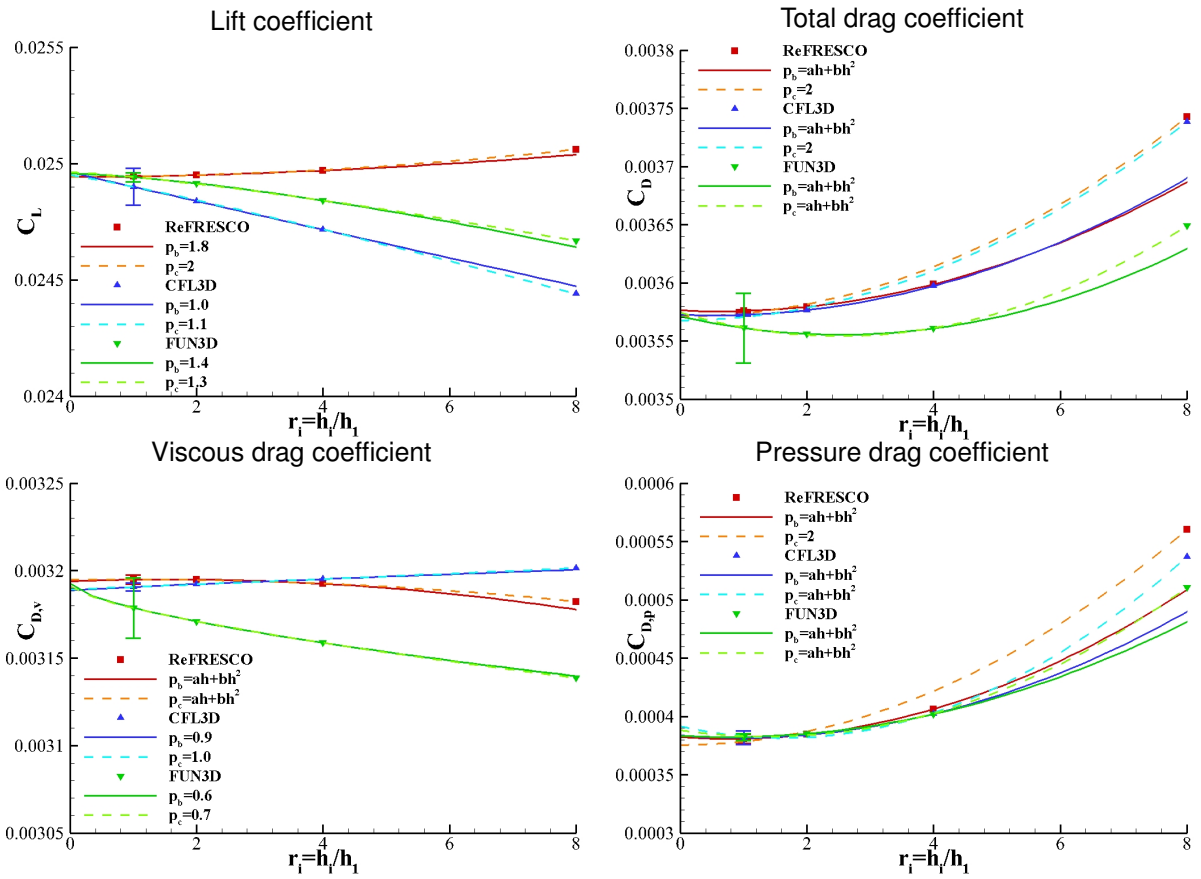

Figure 4.22: Total drag coefficient C_D, lift coefficient C_L, pressure drag coefficient C_{D_v} and viscous drag coefficient C_{D_p} as a function of the grid refinement ratio r_i obtained with ReFRESCO, CFL3D and FUN3D in the N grids set. p_b is obtained from the 3 grids with $r_i = 1$, $r_i = 2$ and $r_i = 4$; p_c is obtained from the 4 grids with $r_i = 1$, $r_i = 2$,$r_i = 4$ and $r_i = 8$. Two-dimensional viscous flow over a bump.

Table 4.7: Observed order of grid convergence p, estimated exact solution C_{L_o} and the absolute difference of C_{f_o} computed by ReFRESCO and the one obtained with the other solvers $|\Delta C_{L_o}|$ relative to ReFRESCO solutions, of the lift coefficient obtained with ReFRESCO, CFL3D and FUN3D in the N grid set. p_b is obtained from the 3 grids with $r_i = 1$, $r_i = 2$ and $r_i = 4$; p_c is obtained from the 4 grids with $r_i = 1$, $r_i = 2$,$r_i = 4$. Two-dimensional viscous flow over a bump.

		ReFRESCO	CFL3D	FUN3D
p	b	1.79	0.49	1.44
	c	fixed 2nd order (eq. 3.5b)	1.13	1.28
C_{L_o}	b	2.4942×10^{-2}	2.4963×10^{-2}	2.4957×10^{-2}
	c	2.4943×10^{-2}	2.4949×10^{-2}	2.4962×10^{-2}
$\lvert\Delta C_{L_o}\rvert$	b	-	0.084%	0.060%
	c	-	0.024%	0.076%

This is evidenced by the fact that, while the results of ReFRESCO for the left-side plot are very similar to the comparative data regarding the extrapolated solution (if the solution from the gird with $r_i = 8$ is not included), while the plot on the right shows differences on the extrapolated solutions as high as 0.232% for the three most refined grids. However, even those, are in the sixth decimal figure of C_f.

Table 4.8: Observed order of grid convergence p, estimated exact solution C_{D_o} and the absolute difference of C_{f_o} computed by ReFRESCO and the one obtained with the other solvers $|\Delta C_{D_o}|$ relative to ReFRESCO solutions, of the total drag coefficient obtained with ReFRESCO, CFL3D and FUN3D in the N grid set. p_b is obtained from the 3 grids with $r_i = 1$, $r_i = 2$ and $r_i = 4$; p_c is obtained from the 4 grids with $r_i = 1$, $r_i = 2$,$r_i = 4$. Two-dimensional viscous flow over a bump.

		ReFRESCO	CFL3D	FUN3D
p	b	2 terms expansion (eq. 3.5c)	2 terms expansion (eq. 3.5c)	2 terms expansion (eq. 3.5c)
	c	fixed 2nd order (eq. 3.5b)	fixed 2nd order (eq. 3.5b)	2 terms expansion (eq. 3.5c)
C_{D_o}	b	3.5762×10^{-3}	3.5726×10^{-3}	3.5710×10^{-3}
	c	3.5709×10^{-3}	3.5678×10^{-3}	3.5744×10^{-3}
$\|\Delta C_{D_o}\|$	b	-	0.101%	0.145%
	c	-	0.087%	0.098%

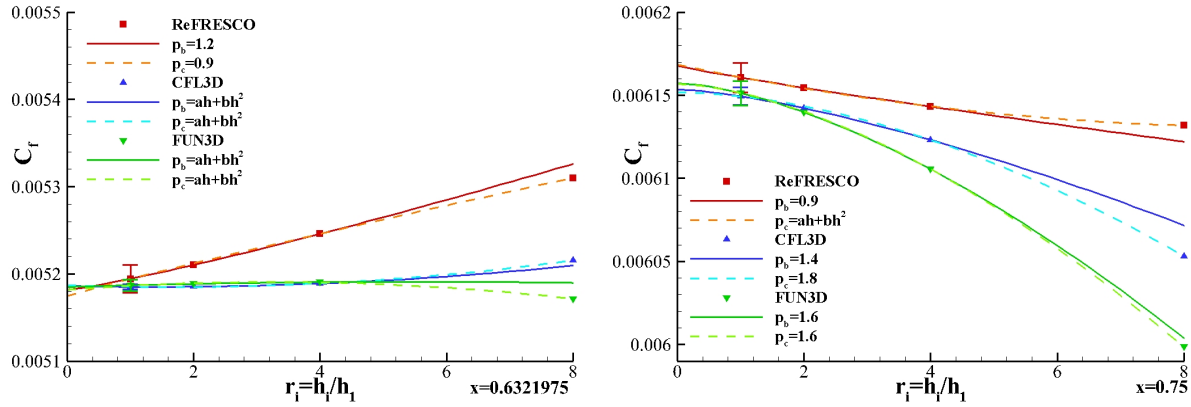

Figure 4.23: Skin friction coefficient C_f at $x = 0.6321975m$ and at $x = 0.75m$ as a function of the grid refinement ratio r_i obtained with ReFRESCO, CFL3D and FUN3D in the N grids set. p_b is obtained from the 3 grids with $r_i = 1$, $r_i = 2$ and $r_i = 4$; p_c is obtained from the 4 grids with $r_i = 1$, $r_i = 2$,$r_i = 4$ and $r_i = 8$. Two-dimensional viscous flow over a bump.

Table 4.9: Observed order of grid convergence p, estimated exact solution C_{f_o} and the absolute difference of C_{f_o} computed by ReFRESCO and the one obtained with the other solvers $|\Delta C_{f_o}|$ relative to ReFRESCO solutions, of the skin friction coefficient at $x = 0.6321975m$ obtained with ReFRESCO, CFL3D and FUN3D in the N grid set. p_b is obtained from the 3 grids with $r_i = 1$, $r_i = 2$ and $r_i = 4$; p_c is obtained from the 4 grids with $r_i = 1$, $r_i = 2$,$r_i = 4$. Two-dimensional viscous flow over a bump.

		ReFRESCO	CFL3D	FUN3D
p	b	1.17	2 terms expansion (eq. 3.5c)	2 terms expansion (eq. 3.5c)
	c	0.93	2 terms expansion (eq. 3.5c)	2 terms expansion (eq. 3.5c)
C_{f_o}	b	5.1814×10^{-3}	5.1861×10^{-3}	5.1848×10^{-3}
	c	5.1848×10^{-3}	5.1871×10^{-3}	5.1818×10^{-3}
$\|\Delta C_{f_o}\|$	b	-	0.091%	0.066%
	c	-	0.245%	0.143%

2D NACA0012 Airfoil

The results for the skin friction coefficient on the upper surface of the foil and pressure coefficient distribution on both sides computed in the second finest grid ($r_i = 2.0$) of set N with ReFRESCO for the three angles of attack studied are presented in figure 4.24. The figure also illustrates the reported results

Table 4.10: Observed order of grid convergence p, estimated exact solution C_{f_o} and the absolute difference of C_{f_o} computed by ReFRESCO and the one obtained with the other solvers $|\Delta C_{f_o}|$ relative to ReFRESCO solutions, of the skin friction coefficient at $x = 0.75m$ obtained with ReFRESCO, CFL3D and FUN3D in the N grid set. p_b is obtained from the 3 grids with $r_i = 1$, $r_i = 2$ and $r_i = 4$; p_c is obtained from the 4 grids with $r_i = 1$, $r_i = 2$,$r_i = 4$. Two-dimensional viscous flow over a bump.

		ReFRESCO	CFL3D	FUN3D
p	b	0.89	1.43	1.57
	c	2 terms expansion (eq. 3.5c)	1.78	1.63
C_{f_o}	b	6.1679×10^{-3}	6.1536×10^{-3}	6.1573×10^{-3}
	c	6.1685×10^{-3}	6.1518×10^{-3}	6.1567×10^{-3}
$\lvert\Delta C_{f_o}\rvert$	b	-	0.232%	0.172%
	c	-	0.271%	0.191%

for CFL3D solver and the experimental data from two sources: Ladson, et al. [47], with $Re_c = 6 \times 10^6$; and Gregory, et al. [46], with $Re_c \approx 3 \times 10^6$. All the comparative data are taken from [42].

The solutions of ReFRESCO are in great agreement with the results from CFL3D flow solver across all angles of attack for both quantities. Both codes predict a separation bubble in the upper surface of the foil at approximately $x/c = 92\%$ for $\alpha = 15^o$. Similar to the trends in the viscous bump test case, the main discrepancy between ReFRESCO and CFL3D is in the numerical influences of the change in boundary conditions in the trailing edge of the foil.

The experimental data reported in [46] seems to be in line to the CFD solutions despite the difference in the Reynolds number. However, the results obtained by Ladson, and co-workers [47], for $Re_c = 6 \times 10^6$ show considerable differences in the pressure peaks at the leading edge and in pressure levels across the first half of the upper surface. It is believed that these results may not sufficiently represent a two-dimensional flow because the aspect ratio of model used was only 1.333, as stated in [42].

Throughout this sub-section, the results from ReFRESCO were interpolated to same locations as those of the CFL3D solutions using a third-order cubic interpolation. However, if the values of the skin friction coefficient are taken directly form the cell faces that discretize the airfoil surface, oscillations in C_f appear in the upper surface of the foil (or both surfaces if $\alpha = 0^o$).

Figure 4.25 depicts the oscillations for $\alpha = 0^o$. Those are present in all grids of the NACA0012 set and are after the C_f peak. On the other hand, for $\alpha = 10^o$ and $\alpha = 15^o$, the oscillations are moved to the front of the peak. The origin for these anomalous behaviour might be related with the grid properties close to the leading edge of the airfoil. Figure 4.25 also includes a zoom of that region in the grid with $r_i = 4.0$. The increase in eccentricity of the cells, as the grid lines stop to be perpendicular to the airfoil surface, might be the origin of the oscillations.

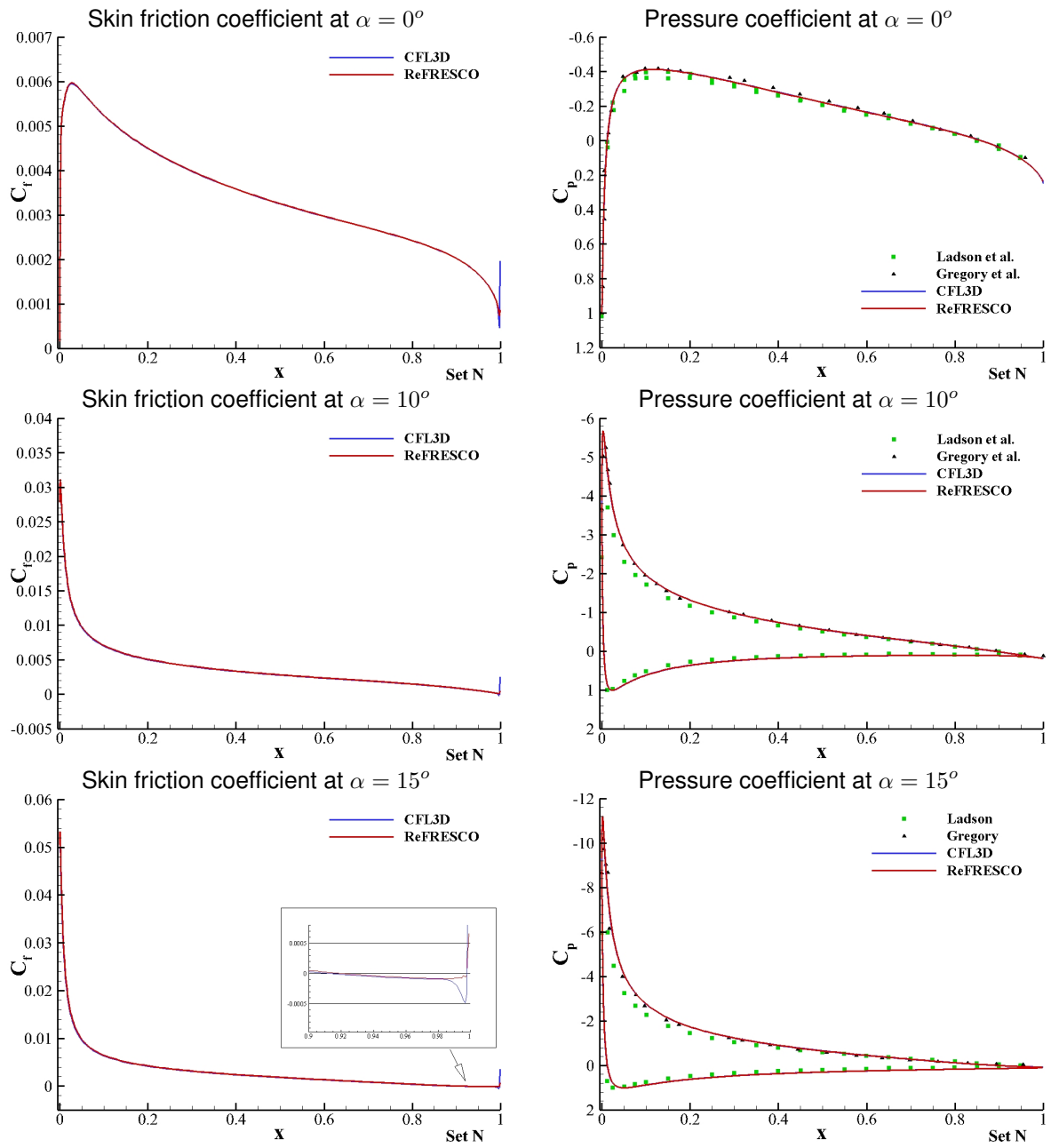

Figure 4.24: Skin friction coefficient C_f of the upper surface and pressure coefficient C_p along both sides of the airfoil obtained with ReFRESCO, CFL3D in the grid with $r_i = 2.0$ of set N. Experimental data from Ladson et al. [47] with $Re_c = 6 \times 10^6$ and tripped transition, and Gregory et al. [46] with $Re_c \approx 3 \times 10^6$, are also included. Two-dimensional flow over the NACA0012 airfoil.

4.4.2 Inviscid flow

The literature comparison for the inviscid bump test cases will be exclusively restricted to the distributions of the Mach number distributions on the top and bottom walls (see section 4.1.2) of the subsonic, transonic, and supersonic flow conditions. As a result, this sub-section is categorized according to the inlet flow regime. Additionally, only the grids with similar cell densities to the ones used in [4] and [9] will be presented. In the former reference, simulations were performed using the TVD SMART scheme for the convective terms discretization, while in the latter the CDS blended with 10% UP was employed

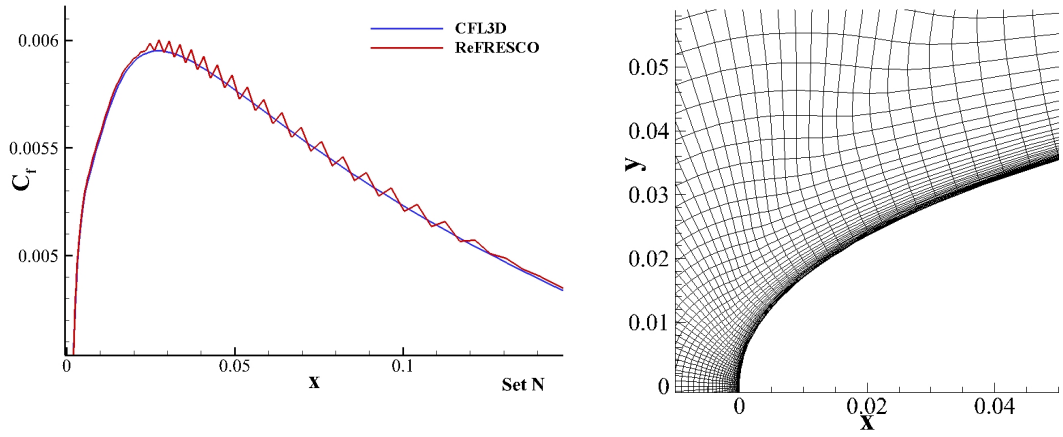

Figure 4.25: Oscillations in the skin friction coefficient C_f on the upper surface of the airfoil (on the left). The solution of ReFRESCO was not interpolated to the locations of the CFL3D results. Instead, the values of C_f taken from every cell face that discretize the airfoil surface on the grid with $r_i = 2$. One the right, a close-up view of the third most refined grid close to the leading edge of airfoil. Two-dimensional flow over the NACA0012 airfoil.

to approximate the convective fluxes. Unfortunately, only visual representations of Mach number distributions were found in the open literature which narrows down the comparative assessment for this test case to a qualitative graphical comparison.

Subsonic flow

So, figure 4.26 presents the Mach number distributions along the top (dashed lines) and the lower boundary (solid lines) obtained with ReFRESCO for the HARM scheme and blended CDS. Additionally, the reported results in [4] and [9] are also replicated.

On ReFRESCO results, there is little influence of the discretization convection scheme. As expected, the largest differences are concerned with the resolution of the geometric singularities, at the start and end of the bump, which deteriorates with grid coarsening. Furthermore, the solution asymmetry is also more noticeable in the coarser grids and is tied to the positive values of C_X in figure 4.14, which is theoretically expected to be zero. However, the distributions of ReFRESCO are similar to those found in the open literature.

Transonic flow

Equivalent results to the previous figure are shown in figure 4.27, but for the transonic flow conditions. Firstly, the confirmation that the numerical settings chosen for these simulations give rise to transonic flow conditions since, at the inlet, $Ma < 1$, then reaches values close $Ma = 1.5$ on the bump surface, and a shock restores subsonic conditions at the outlet of the domain.

Contrary to the behaviour observed in the subsonic conditions, here the choice of convection schemes is more evident. The blended CDS generates oscillations upstream of the shock whereas the HARM

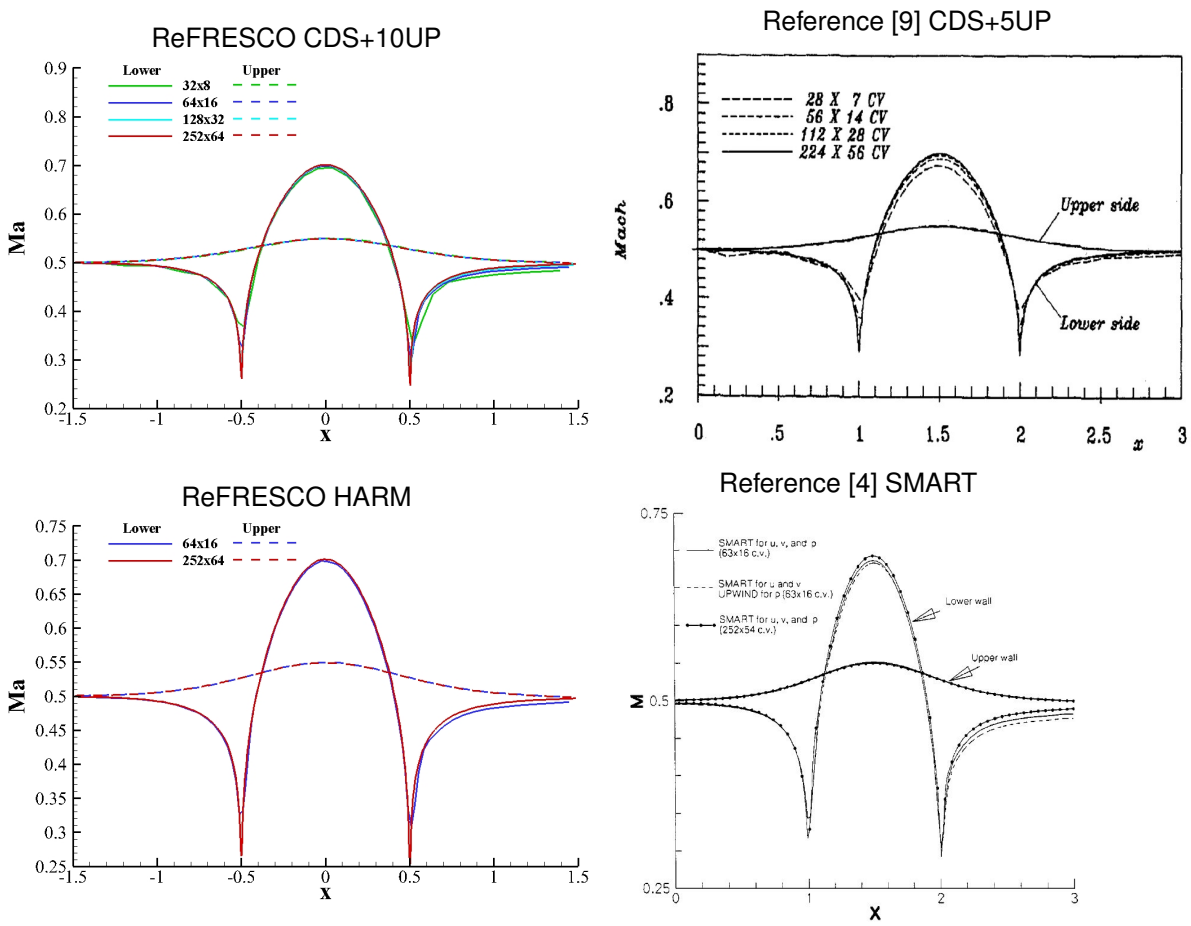

Figure 4.26: Comparison of Mach distributions obtained with ReFRESCO and results available in [9] and [4] for the subsonic flow of an inviscid fluid over a bump. Mach number at the inlet $Ma = 0.5$.

scheme shows a smooth solution. Oscillations are also present after the shock discontinuity, although this time, for both schemes. However, those typically affect the same number of cells thus the region affected by these numerical oscillations tends to decrease with grid refinement.

The results from ReFRESCO and the two reference solutions in figure 4.27 are generally in good agreement. Although the results from [9] do not show oscillations upstream of the shock wave, despite being computed with the same numerical convection scheme, it is assumed that their vanishing is tied to the grid spacing on that region. Nonetheless, all numerical simulations exhibit oscillations after the shock wave roughly at the same locations between them.

Supersonic flow

The last test case of this section will consider the Mach distributions on the upper and lower sides of the domain in supersonic conditions. Those are illustrated in figure 4.28 for the solution obtained with ReFRESCO, and reported in [4] and [9] alike. The flow, in fact, is fully supersonic, i.e. $Ma > 1$ throughout both walls, which validates changing the pressure imposition boundary condition to the inlet over the outlet of the domain (see section 3.1.2).

Among the three undisturbed flow Mach number, the present one is the more demanding for the accuracy of the solution. Two oblique shocks are generated, at the leading and trailing edges of the

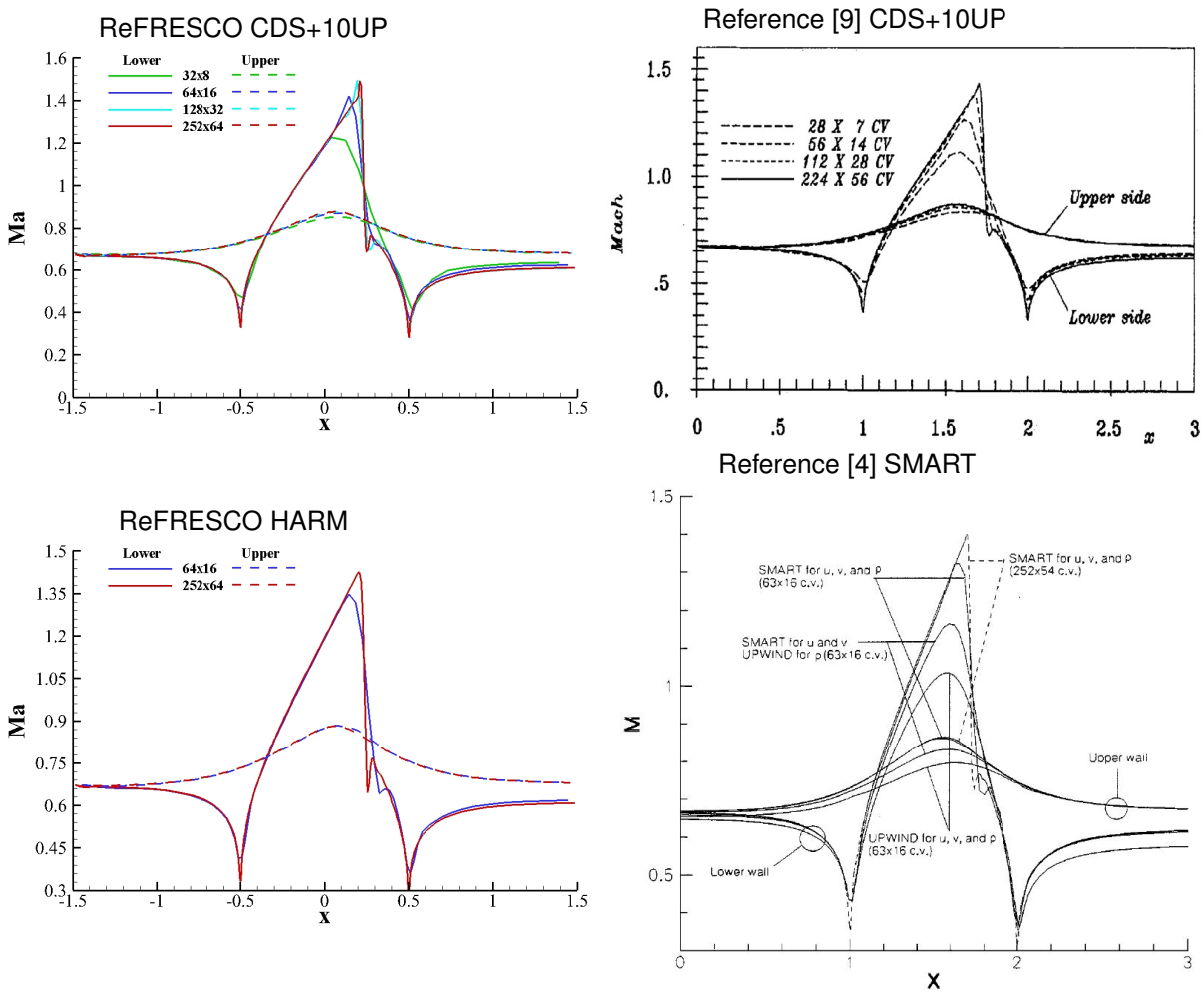

Figure 4.27: Comparison of Mach distributions obtained with ReFRESCO and results available in [9] and [4] for the transonic flow of an inviscid fluid over a bump. Mach number at the inlet $Ma = 0.675$.

bump, and the first is reflected on the top wall where the effect of grid coarsening is more negetivly felt. Moreover, using the blended CDS for convective fluxes results in more oscillations than using the HARM scheme. The behaviour and value of the Mach number at the outlet boundary is also depedent on the grid refinment level and on the convection scheme, as it was seen in figure 4.16.

When comparing with results available in the open literature, the biggest discrepancy in the ReFRESCO solutions are felt using the CDS, more precisely after the oblique shocks. However, in [9] it was assumed constant stagnation temperature, so T is directly computed from equation 2.11a, whereas the present simulations of ReFRESCO solve the energy equation (eq.2.1c). Note that, contrary to the transonic flow simulations, the solutions reported in [9] show oscillations prior to the geometric discontinuities which favours the assumption made in the previous flow regime.

Admittedly, the comparison between ReFRESCO and [4] can be inconclusive since the convection schemes are not the same (although they are both TVD schemes) and the grid set is not equal, both in density and in grid spacing. Nonetheless, common trends can be found in both solutions, like the oscillations at the back of the shocks.

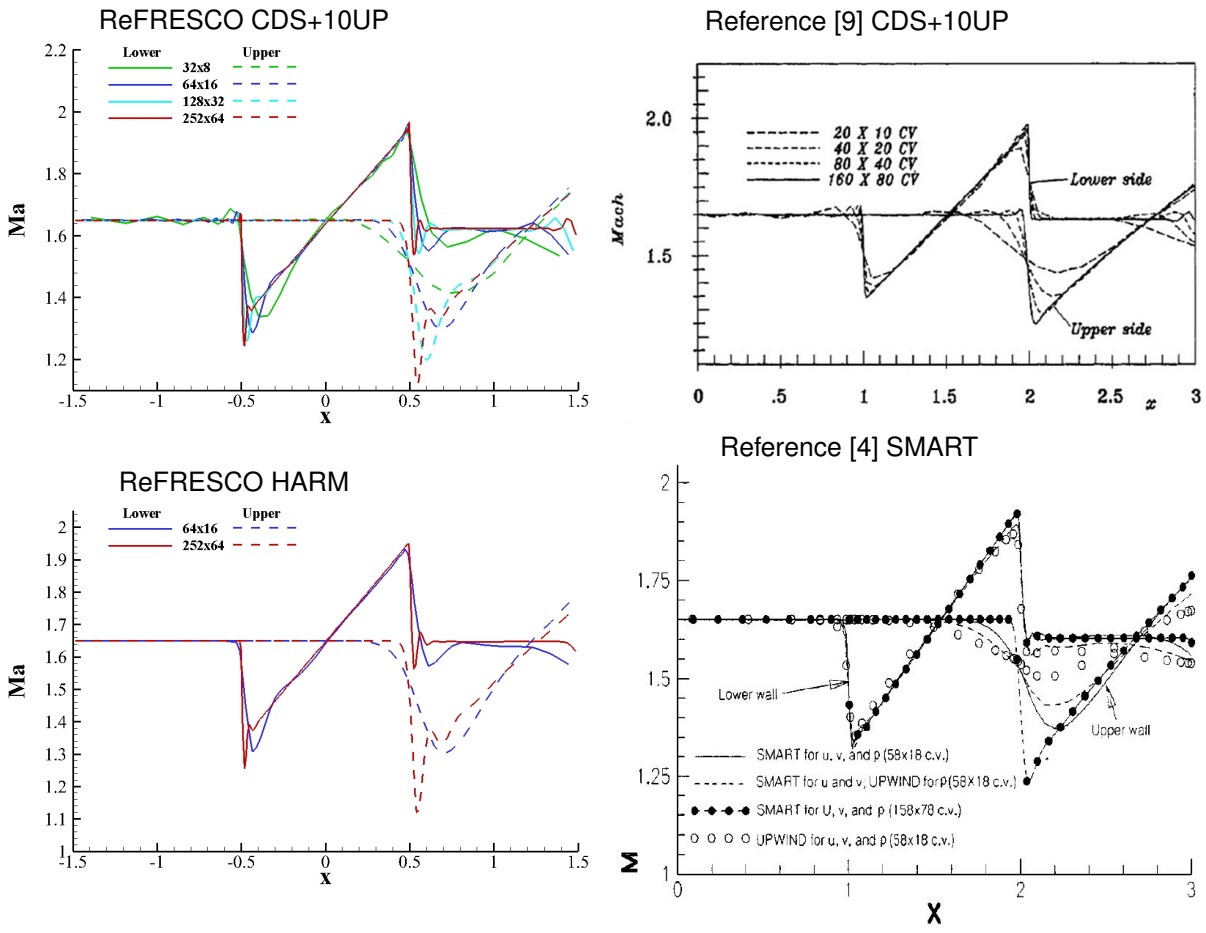

Figure 4.28: Comparison of Mach distributions obtained with ReFRESCO and results available in [9] and [4] for the supersonic flow of an inviscid fluid over a bump. Mach number at the inlet $Ma = 1.65$.

Chapter 5

Conclusions

In this thesis, a study of the robustness and accuracy of the single-phase, pressure-based, compressible flow solver in ReFRESCO, was performed. The iterative and discretization convergence properties were analysed in six different two-dimensional test cases: viscous flow over a plate, a bump and the NACA0012 airfoil; and inviscid flow over a bump in subsonic, transonic and supersonic regimes. The first three test cases are described in the NASA Turbulence Resource Modeling website [18], while the remaining ones are commonly found in the open literature as benchmark cases for compressible flow solvers [4, 9]. Comparative data was taken from the previous sources to contrast with the solutions obtained by ReFRESCO.

The mathematical model used entails a system of equations composed by the continuity equations, the Navier-Stokes equations, the conservation of total energy principle and an algebraic equation of state, the ideal gas law. Additionally, for a statistically steady turbulent flow, the Favre-average procedure is applied and the system is supplemented with the one-equation turbulence model of Spalart and Allmaras. ReFRESCO uses a finite-volume method formulation to discretize the governing flow equations, together with a segregated approach using a SIMPLE-like algorithm for the solution procedure.

The estimation of the discretization error was performed with grid refinement studies using different sets of geometrically similar grids. The sets for the viscous flow test cases are available at [18]. Only the flat plate case study feature an alternative set using multi-block structured grids and two extra grids were added to the original set. For the inviscid bump test case, a set of single-block structured grids covers not only the typical grid densities found in the open literature, but also sufficiently fine grids necessary to obtain mostly monotonic convergent solutions for the quantities of interest studied.

The main conclusion to derive from the results of this work were:

- The compressible flow solver is robust. From the 45 unique grids used, only in the sparsest grid of the NACA0012 an iteratively converged solution to the non-linear problem was not obtained. Additionally, the residuals of the non-linear problem were converged to values close to machine accuracy, again, only in the NACA0012 airfoil test case the stopping criteria was increased on order of magnitude due to time constraints. Nonetheless, it was found that iterative convergence of the non-linear residual is influenced by the following:

  - Insufficiently converged solutions of the linear system of equations that solve the pressure-correction equation may originate highly irregular behaviour of the non-linear convergence;
  - The use of direct solvers in the linear system of equations also eliminates those irregularities but does not guarantee lower simulation times over iterative solvers;
  - The convergence rate of the non-linear problem degrades with the increase of grid density as fine grids require smaller values of the under-relaxation parameters. Nonetheless, the use of an improved initial condition for the iterative process, like interpolating a converged solution from a coarser grid, allows a selection of higher values of under-relaxation parameters as divergence in the earlier stages of convergence is less likely;
  - The inlet flow regime also influences the choice of the under-relaxation parameters with the transonic conditions being more demanding on the solver robustness. Nonetheless, iterative convergence rates for the inviscid bump test case are similar to those found in the open literature for the three flow regimes;
  - Another grid characteristic that greatly affects the rate of convergence is extending the near-wall cell size at the solid surfaces to the wake region. Such small cells in that region greatly increases the diffusivity and slows down considerably the convergence rate as the residuals are converged close to machine accuracy.

- Grid convergence properties are dependent on the convection scheme, inlet flow regime, quantity of interest and incoming flow angle of attack.

- Concerning the inviscid flow test case, estimations of the exact solution are not always consistent between the four convection schemes. This is mostly evidenced in the supersonic test case. The discrepancies are tied to the loss of stagnation temperature (that should remain constant) due to the geometric singularities and shocks. However, the pressure is consistent across all schemes.

- ReFRESCO yields consistent solutions in the two grid sets of the flat plate exercise, i.e. the error bars obtained for the two finest grids solutions intersect. However, there are key factors to take into consideration when performing any Solution Verification exercise:

  - Ensure that the solutions are obtained in sufficiently fine grids for the data set to be in the asymptotic range. Often times, the typical grid densities employed in the open literature lack resolution for reliable estimates of grid convergence properties;
  - Careful selection of the residual stopping criteria is mandatory. Lack of iterative convergence generates misleading solutions. The inevitable data scattering is evidenced in grid convergence exercises by an increase of the numerical uncertainty. To ensure negligible influence of the iterative error, not only the residuals, but also the changes of variables between each consecutive iteration should converge to values close to machine accuracy. Attention to these aspects is rewarded with mostly close to second-order convergence levels for integral quantities and slightly lower values for local flow quantities.

- The solutions obtained with ReFRESCO are in great graphical agreement with solutions from other CFD solvers, like CFL3D and FUN3D. However, some differences between the solutions of the three solvers are higher than the estimated numerical uncertainty of ReFRESCO. More definitive statements concerning the consistency of ReFRESCO are only possible if information regarding the uncertainty of the comparative data is available.
- Moreover, ReFRESCO accurately predicts solutions in subsonic, transonic and supersonic conditions, when comparing to other pressure-based solvers. However, oscillations can appear close to geometrical singularities, shocks and in poor quality (excessive eccentricity) grids.

Future Work

Initially, this thesis was planned to include a Solution Verification exercise considering a three-dimensional test case. However, ensuring that the ´studied solutions had negligible influence of the iterative error always took precedence. Not only that but, the number of cells of the finest grids used in this study are considerably high (close to 1 million for most of them). These facts, combined with limited hardware capabilities, resulted in simulation runs that took approximately 1 week to conclude. Nonetheless, more reliable conclusions can be derived from the viscous bump and NACA0012 test cases, if extra grids are added to their sets (like in the flat plate test case). Additionally, for the airfoil case study, lower iterative convergence criteria should also be considered. However, the present version of the single-phase compressible solver in ReFRESCO is only an intermediate step towards the end-goal, be able to handle multi-phase compressible flows. This, in turn, would imply re-evaluation of numerical properties with different test cases that simulate relevant phenomena of multi-phase compressible fluids.

Bibliography

[1] J. Tu, G. H. Yeoh, and C. Liu. *Computational fluid dynamics: a practical approach*. Butterworth-Heinemann, 2018.

[2] F. Moukalled, L. Mangani, and M. Darwish. *The Finite Volume Method in Computational Fluid Dynamics An Advanced Introduction with OpenFOAM and Matlab*. Springer, 1 edition, 2016. ISBN 9781402067419. URL http://www.springer.com/series/5980.

[3] J. D. Anderson Jr. *Fundamentals of aerodynamics*. Tata McGraw-Hill Education, 2010.

[4] F. Moukalled and M. Darwish. A High-Resolution Pressure-Based Algorithm for Fluid Flow at All Speeds. *Journal of Computational Physics*, 168(1):101 – 130, 2001. ISSN 0021-9991. doi: https://doi.org/10.1006/jcph.2000.6683. URL http://www.sciencedirect.com/science/article/pii/S002199910096683X.

[5] A. Jameson, W. Schmidt, and E. Turkel. Numerical solution of the Euler equations by finite volume methods using Runge Kutta time stepping schemes. In *14th Fluid and Plasma Dynamics Conference*, volume M, pages 1–19, Reston, Virigina, jun 1981. American Institute of Aeronautics and Astronautics. ISBN 9781441976314. doi: 10.2514/6.1981-1259. URL http://arc.aiaa.org/doi/10.2514/6.1981-1259.

[6] S. V. Patankar and D. B. Spalding. A calculation procedure for heat, mass and momentum transfer in three-dimensional parabolic flows. *International Journal of Heat and Mass Transfer*, 15(10):1787–1806, 1972. ISSN 00179310. doi: 10.1016/0017-9310(72)90054-3.

[7] G. Raithby and J. Van Doormaal. Enhancements of the simple method for predicting incompressible fluid flows. *Numer. Heat Transfer*, 7(2):147–163, 1984.

[8] S. Patankar. Calculation of unsteady compressible flows involving shocks. *Mechanical Engineering Department, HTS/71/28, Imperial College*, 1971.

[9] I. Demirdžić, ž. Lilek, and M. Perić. A Collocated Finite Volume Method For Predicting Flows at All Speed. *Journal of Numerical Methods in Fluids*, 16(12):1029–1050, 1993. ISSN 10970363. doi: 10.1002/fld.1650161202.

[10] K. C. Karki and S. V. Patankar. Pressure based calculation procedure for viscous flows at all speeds in arbitrary configurations. *AIAA Journal*, 27(9):1167–1174, 1989. doi: 10.2514/3.10242.

[11] J. H. Ferziger and M. Perić. *Computational Methods for Fluid Dynamics*. Springer-Verlag GmbH, 3rd edition, 2001. ISBN 3540420746.

[12] A. Rizzi and L.-E. Eriksson. Computation of inviscid incompressible flow with rotation. *Journal of Fluid Mechanics*, 153:275–312, 1985.

[13] J. M. Weiss and W. A. Smith. Preconditioning applied to variable and constant density flows. *AIAA journal*, 33(11):2050–2057, 1995.

[14] L. E. J. Muralha and C. Klaij. Application of the simple algorithm to a manufactured subsonic flow. In *21st Numerical Towing Tank Symposium, NuTTS 2018*, 2018.

[15] L. E. J. Muralha and C. Klaij. Assessing refresco compressible single phase flow solver numerical robustness. In *22nd Numerical Towing Tank Symposium, NuTTS 2019*, 2019.

[16] Marin. Refresco, 2020. URL `www.refresco.org`.

[17] P. J. Roache. Code Verification by the Method of Manufactured Solutions. *J Fluid Eng*, 124 (1):4, 2002. ISSN 00982202. doi: 10.1115/1.1436090. URL `http://fluidsengineering.asmedigitalcollection.asme.org/article.aspx?articleid=1429463`.

[18] C. Rumsey. Langley Research Center Turbulence Modeling Resource, 2020. URL `https://turbmodels.larc.nasa.gov/`.

[19] P. J. Roache. *Verification and Validation in Computational Science and Engineering*. Hermosa Pub, 1998. ISBN 0913478083.

[20] L. Eça and M. Hoekstra. A procedure for the estimation of the numerical uncertainty of CFD calculations based on grid refinement studies. *Journal of Computational Physics*, 262:104–130, 2014.

[21] D. C. Wilcox. *Turbulence Modeling for CFD*. DCW Industries, 3rd edition, 2006.

[22] V. Brederode. *Fundamentos de aerodinâmica imcompressível*. Author's Edition, 1997.

[23] H. Schlichting. *Boundary layer theory*. Springer, 1968.

[24] A. S. Spalart P.R. A One-Equation Turbulence Model for Aerodynamic Flows. In *AIAA 30$^{\text{th}}$ Aerospace Sciences Meeting, Reno, U.S.A.*, 1992.

[25] F. Menter. Review of the shear-stress transport turbulence model experience from an industrial perspective. *International journal of computational fluid dynamics*, 23(4):305–316, 2009.

[26] W. Jones and B. Launder. The prediction of laminarization with a two-equation model of turbulence. *International journal of heat and mass transfer*, 15(2):301–314, 1972.

[27] D. Wilcox. Reassessment of the scale-determining equation for advanced turbulence models. *AIAA journal*, 26(11):1299–1310, 1988.

[28] C. Rumsey. The spalart-allmaras turbulence model, 2020. URL https://turbmodels.larc.nasa.gov/spalart.html.

[29] F. Moukalled, L. Mangani, and M. Darwish. Implementation of boundary conditions in the finite-volume pressure-based method—Part I: Segregated solvers. *Numerical Heat Transfer, Part B: Fundamentals*, 69(6):534–562, jun 2016. ISSN 1040-7790. doi: 10.1080/10407790.2016.1138748. URL http://www.tandfonline.com/doi/full/10.1080/10407790.2016.1138748.

[30] F. Moukalled, L. Mangani, and M. Darwish. The characteristic boundary condition in pressure-based methods. *Numerical Heat Transfer, Part B: Fundamentals*, 76(2):43–59, aug 2019. ISSN 1040-7790. doi: 10.1080/10407790.2019.1644942. URL https://doi.org/10.1080/10407790.2019.1644942https://www.tandfonline.com/doi/full/10.1080/10407790.2019.1644942.

[31] C. Silva, J. Muralha, L. Eça, and C. Klaij. Assessment of the Numerical Properties of ReFRESCO Pressure Based Compressible Flow Solver : Flow over a Flat Plate. Technical Report July, IST, 2020.

[32] J. Muralha, L. Eça, and C. M. Klaij. Code verification of a pressure-based solver for subsonic compressible flows. *J. Verif. Valid. Uncert.*, 5(4):041001, 2020. URL https://doi.org/10.1115/1.4048750.

[33] C. Hirsch. *Numerical computation of internal and external flows: The fundamentals of computational fluid dynamics*. Elsevier, 2007.

[34] S. Balay, S. Abhyankar, M. F. Adams, J. Brown, P. Brune, K. Buschelman, L. Dalcin, A. Dener, V. Eijkhout, W. D. Gropp, D. Karpeyev, D. Kaushik, M. G. Knepley, D. A. May, L. C. McInnes, R. T. Mills, T. Munson, K. Rupp, P. Sanan, B. F. Smith, S. Zampini, H. Zhang, and H. Zhang. PETSc Web page. https://www.mcs.anl.gov/petsc, 2019. URL https://www.mcs.anl.gov/petsc.

[35] Waterson, Nicholas P. and Deconinck, Herman. Design Principles for Bounded Higher-Order Convection Schemes–a Unified Approach. *Journal of Computational Physics*, 224(1):182–207, 2007.

[36] H. M. *Numerical Simulation of Ship Stern Flows with a Space-Marching Navier-Stokes Method*. PhD thesis, University of Delft, 1999.

[37] E. L., P. F.S., and V. G. Viscous flow simulations at high reynolds numbers without wall functions: Is $y^+ \simeq 1$ enough for the near-wall cells? *Computers & Fluids*, 170:157–175, jul 2018. ISSN 00457930. doi: 10.1016/j.compfluid.2018.04.035. URL https://linkinghub.elsevier.com/retrieve/pii/S0045793018302299.

[38] W. J. Eça L., Hoekstra M. Practical Grid Generation Tools with Applications to Ship Hydrodynamics. In *8$^{\text{th}}$ International Conference on Numerical Grid Generation in Computational Field Simulations, Honolulu, Hawaii, U.S.A.*, 2002.

[39] C. Rumsey. VERIF/2DZP: 2D Zero Pressure Gradient Flat Plate Verification Case - Intro Page, 2020. URL https://turbmodels.larc.nasa.gov/flatplate.html.

[40] C. Rumsey. VERIF/2DB: 2D Bump-in-channel Verification Case - Intro Page, 2020. URL https://turbmodels.larc.nasa.gov/bump.html.

[41] C. Rumsey. Grids - 2D Bump-in-channel Verification Case, 2020. URL https://turbmodels.larc.nasa.gov/bump{_}grids.html.

[42] C. Rumsey. 2DN00: 2D NACA 0012 Airfoil Validation Case, 2020. URL https://turbmodels.larc.nasa.gov/naca0012{_}val.html.

[43] C. Rumsey. Grids - NACA 0012 Airfoil Case, 2020. URL https://turbmodels.larc.nasa.gov/naca0012{_}grids.html.

[44] C. Rumsey. CFL3D Version 6.7, 2017. URL https://cfl3d.larc.nasa.gov/.

[45] E. Lee-Rausch. FUN3D: Fully Unstructured Navier-Stokes, 2020. URL https://fun3d.larc.nasa.gov/.

[46] N. Gregory and C. L. O'Reilly. Low-Speed Aerodynamic Characteristics of NACA 0012 Aerofoil Sections, including the Effects of Upper-Surface Roughness Simulation Hoar Frost. Technical Report 3726, NPL AERO, January 1970.

[47] C. L. Ladson, A. S. Hill, and W. G. Johnson, Jr. Pressure Distributions from High Reynolds Number Transonic Tests of an NACA 0012 Airfoil in the Langley 0.3-Meter Transonic Cryogenic Tunnel. Technical Report TM-100526, NASA, December 1987.

[48] C. Rumsey. SA Expected Results - 2D Zero Pressure Gradient Flat Plate, 2020. URL https://turbmodels.larc.nasa.gov/flatplate{_}sa.html.

[49] C. Rumsey. Grids - 2D Zero Pressure Gradient Flat Plate Verification Case, 2020. URL https://turbmodels.larc.nasa.gov/flatplate{_}grids.html.

[50] C. Rumsey. SA Expected Results - 2D Bump-in-channel, 2020. URL https://turbmodels.larc.nasa.gov/bump{_}sa.html.

Appendix A

Alternative grid set for the viscous bump test case

This appendix presents the results for an alternative grid set generated for the viscous bump test case conditions presented in figure 3.3. The set is composed of 5 multi-block geometrically similar grids. Here, the grids lines are locally orthogonal and parallel to the entire wall boundary surface, both plate and bump. However, those recover Cartesian orientation at $0.3m$ above the lower boundary. The clustering of cells at the leading edge of the horizontal plate extends to the trailing edge. Afterwards, an expansion of the grid lines guarantees no excessively small cells at the wake that hinder iterative convergence rate, as addressed in sub-section 4.2.1. Figure A.1 illustrates the sparsest grid of this set and table A.1 summarizes some information regarding each grid. Two extra grids (grid a and b) were added to the original set to improve the estimation of convergence properties.

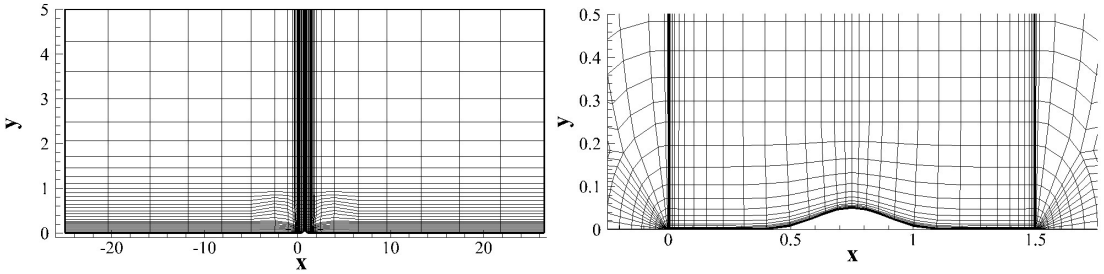

Figure A.1: Illustration of the coarsest grid ($r_i = 16$) of an alternative grid set generated for the two-dimensional viscous flow over a bump test case conditions.

Results

The following solutions were obtained by iteratively converging the non-linear problem until 10^{-8} of the L_∞ norm of the normalized residuals. Figure A.2 presents the skin friction distribution on the plate+bump solid surface on the finest grid of this set, red colour lines. For reference, the green lines represent the solutions of the finest of set N (of the 2D bump-in.channel test case). Naturally, all results presented here were obtained with compressible flow solver in ReFRESCO.

Table A.1: Total number of cells N_{cells}, number of boundary faces in the bump N_{wall} and grid refinement ratio r_i of the grids composing an alternative grid set generated for the two-dimensional viscous flow over a bump test case.

Grid	r_i	N_{cells}	N_{wall}	y^+_{max}
1	1.00	716 800	640	0.447
a	1.43	351 232	448	0.588
2	2.00	179 320	224	0.763
b	2.86	87 808	224	1.00
3	4.00	44 800	160	1.32
4	8.00	11 200	80	2.33
5	16.0	2 800	40	4.30

Overall, the two distributions have good graphical similarities. Exception goes to the oscillations in C_f at the bump's peak, as illustrated in the close-up view, at the right-side of figure A.2. This anomaly greatly influences the evaluation of grid convergence properties for the skin friction coefficient on that location, as it is evidenced in figure A.3.

The left-side depicts the results of grid convergence studies to C_f at $x = 0.6321975$ and the right-side at $x = 0.75$. The red lines are fitted to the solutions of the 5 most refined grids (p_a) of the alternative grid set. While the green fits represent the solutions on set N.

The results for C_f are consistent in the two selected locations, i.e. the uncertainty bars overlap. However, the oscillation in figure A.3 results in a constant overestimation of C_f and loss of monotonic convergence, despite the use of finer grids. Furthermore, the disparities of the the extrapolated solutions are also aggravated. The opposite behaviour is found in the left-side plot which emphasizes the local impact of this anomaly.

The oscillation in C_f is present in all grids of the alternative set. Its origin was found to be related to the increase in eccentricity of the cells around the bump's peak. If a cell centre (instead of a cell face) is at $x = 0.75m$ the oscillation of C_f vanishes.

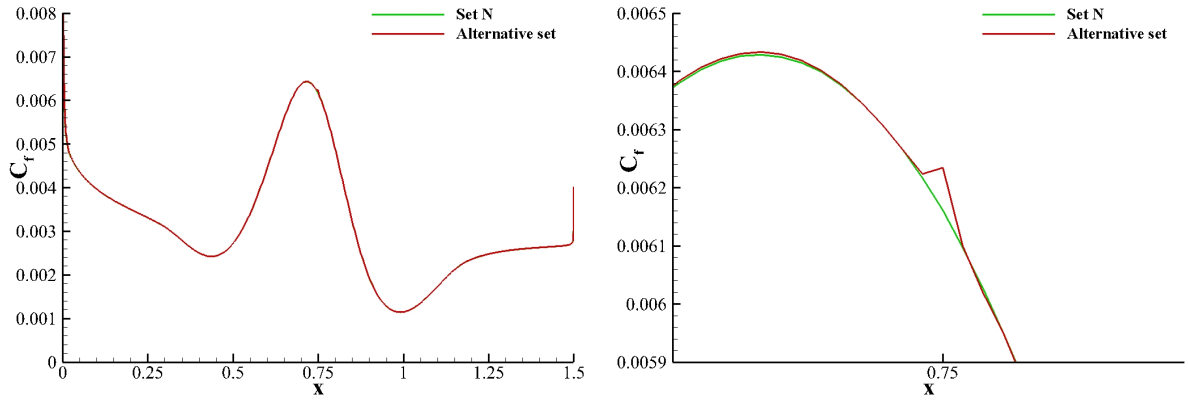

Figure A.2: Skin friction coefficient C_f along the solid surface (plate+bump) obtained with ReFRESCO. The green lines represent the solution on the finest grid of set N of the 2D bump-in-channel test case, while the red colour lines illustrate the solution on the finest grid of the alternative set.

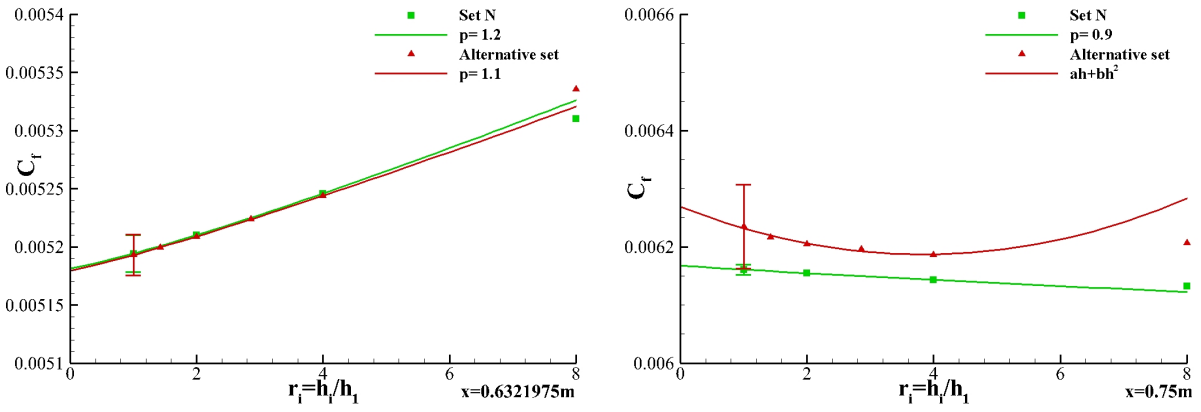

Figure A.3: Grid convergence studies to the skin friction coefficient C_f at $x = 0.6321975$ (left-side) and at $x = 0.75$ (right-side). All solutions were obtained with ReFRESCO. The value of p for the red data set is obtained from the 5 grids with $\leq r_i \leq$ of the alternative grid set; the green line if fitted to the solutions of the the grids with $r_i = 1$, $r_i = 2$ and $r_i = 4$ of set N of the 2D bump-in-channel test case.